

**RL-TR-96-216**  
**In-House Report**  
**March 1997**



# **NONLINEAR OPTICAL MATERIALS AND APPLICATIONS**

**George A. Brost**

*APPROVED FOR PUBLIC RELEASE; DISTRIBUTION UNLIMITED.*

**19970429 203**

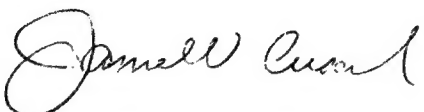
**Rome Laboratory  
Air Force Materiel Command  
Rome, New York**

**DTIC QUALITY INSPECTED 1**

This report has been reviewed by the Rome Laboratory Public Affairs Office (PA) and is releasable to the National Technical Information Service (NTIS). At NTIS it will be releasable to the general public, including foreign nations.

RL-TR-96-216 has been reviewed and is approved for publication.

APPROVED:



JAMES W. CUSACK  
Chief, Photonics Division  
Surveillance & Photonics Directorate

FOR THE COMMANDER:



DONALD W. HANSON, Director  
Surveillance & Photonics Directorate

If your address has changed or if you wish to be removed from the Rome Laboratory mailing list, or if the addressee is no longer employed by your organization, please notify Rome Laboratory/OCPA, Rome, NY 13441. This will assist us in maintaining a current mailing list.

Do not return copies of this report unless contractual obligations or notices on a specific document require that it be returned.

REPORT DOCUMENTATION PAGE			Form Approved OMB No. 0704-0188
<p>Public reporting burden for this collection of information is estimated to average 1 hour per response, including the time for reviewing instructions, searching existing data sources, gathering and maintaining the data needed, and completing and reviewing the collection of information. Send comments regarding this burden estimate or any other aspect of this collection of information, including suggestions for reducing this burden, to Washington Headquarters Services, Directorate for Information Operations and Reports, 1215 Jefferson Davis Highway, Suite 1204, Arlington, VA 22202-4302, and to the Office of Management and Budget, Paperwork Reduction Project (0704-0188), Washington, DC 20503.</p>			
1. AGENCY USE ONLY (Leave blank)	2. REPORT DATE	3. REPORT TYPE AND DATES COVERED	
	March 1997	FINAL, Oct 91 - Sep 95	In-House
4. TITLE AND SUBTITLE <b>NONLINEAR OPTICAL MATERIALS AND APPLICATIONS</b>		5. FUNDING NUMBERS	
		C - NA	PE - 62702F
		PR - 4600	TA - P1
		WU - 11	
6. AUTHOR(S) <b>George A. Brost</b>		8. PERFORMING ORGANIZATION REPORT NUMBER	
7. PERFORMING ORGANIZATION NAME(S) AND ADDRESS(ES) <b>Rome Laboratory/OCPA 25 Electronic Pky Rome NY 13441-4515</b>		8. PERFORMING ORGANIZATION REPORT NUMBER	
9. SPONSORING / MONITORING AGENCY NAME(S) AND ADDRESS(ES) <b>Rome Laboratory/OCPA 25 Electronic Pky Rome NY 13441-4515</b>		10. SPONSORING / MONITORING AGENCY REPORT NUMBER	
		RL-TR-96-216	
11. SUPPLEMENTARY NOTES  <b>Rome Laboratory Project Engineer: George A. Brost, OCPA, (315) 330-7669</b>			
12a. DISTRIBUTION AVAILABILITY STATEMENT  <b>APPROVED FOR PUBLIC RELEASE; DISTRIBUTION UNLIMITED</b>		12b. DISTRIBUTION CODE	
13. ABSTRACT (Maximum 200 words) <b>Characteristics of the photorefractive effect in semiconductors were investigated for applications in optical signal processing. Nonstationary recording techniques of moving gratings and alternating electric fields were examined numerically and experimentally. The dependence on modulation depth was studied in detail. Saturation effects at large modulation limited the enhancement of these nonstationary recording techniques. The photorefractive properties of the II-VI semiconductors ZnTe:Mn:v and Cd<sub>0.55</sub>Mn<sub>0.45</sub>Te:V were characterized. These materials provide good response in the near infrared.</b>			
14. SUBJECT TERMS <b>photorefraction, semiconductors, signal processing</b>		15. NUMBER OF PAGES <b>76</b>	
		16. PRICE CODE	
17. SECURITY CLASSIFICATION OF REPORT <b>UNCLASSIFIED</b>	18. SECURITY CLASSIFICATION OF THIS PAGE <b>UNCLASSIFIED</b>	19. SECURITY CLASSIFICATION OF ABSTRACT <b>UNCLASSIFIED</b>	20. LIMITATION OF ABSTRACT <b>UNLIMITED</b>

## CONTENTS

1. INTRODUCTION	1
2. PHOTORFRACTIVE ACOUSTO-OPTIC ADAPTIVE PROCESSING	2
3. NONSTATIONARY PHOTOREFRACTIVE RECORDING	5
3.1 Numerical Method	6
3.2. Numerical Results	8
3.2.1 Moving Gratings	8
3.2.2. AC Fields	20
3.2.2.1 Modulation Dependence	20
3.2.2.2 Frequency Dependence	24
3.3 Experimental Results	28
3.3.1. Moving Gratings	28
3.3.2 AC Fields	36
3.3.2.1. Modulation Effects	36
3.3.2.2 AC Field Frequency Dependence	39
3.4. Discussion	44
4. STATIONARY RECORDING	45
5. II-VI PHOTOREFRACTIVES	51
5.1 ZnTe	51
5.2 CdMnTe	55
6. SUMMARY	62
REFERENCES	64

## LIST OF FIGURES

	pg.
Fig. 2.1 Experimental layout for photorefractive acousto-optic adaptive processor ....	3
Fig. 3.1a. Calculated amplitude, imaginary component, and phase of the fundamental component of the space-charge field with moving gratings for small modulation .....	11
Fig. 3.1b. Calculated amplitude, imaginary component, and phase of the fundamental component of the space-charge field with moving gratings for $m = 0.2$ .....	12
Fig. 3.1c. Calculated amplitude, imaginary component, and phase of the fundamental component of the space-charge field with moving gratings for $m = 0.6$ .....	13
Fig. 3.1d. Calculated amplitude, imaginary component, and phase of the fundamental component of the space-charge field with moving gratings for $m = 0.9$ .....	14
Fig. 3.2. Calculated imaginary part of the space charge field normalized with respect to $m$ as a function of beam ratio for moving gratings .....	15
Fig. 3.3. Calculated correction function $f(m)$ , as a function of modulation $m$ , for moving gratings.....	16
Fig. 3.4. Correction parameter as a function of the enhancement parameter for moving gratings .....	18
Fig. 3.5. Calculated temporal response versus normalized time for different values of modulation depth for moving gratings .....	19
Fig. 3.6. Calculated correction function versus modulation for ac fields.....	21
Fig. 3.7. Calculated temporal response of the space charge field for different values of modulation depth for ac fields .....	23
Fig. 3.8. Calculated magnitude of the space charge field versus ac frequency for ac fields .....	25
Fig. 3.9. Calculated magnitude and phase of the space charge field versus time over one period of the ac field oscillation at steady state, for $Q = 3$ .....	26

Fig. 3.10. Calculated fluctuation in phase as a function of Q for ac fields .....	27
Fig. 3.11. Experimental setup for two- and four- wave mixing experiments in BSO..	29
Fig. 3.12. Experimental two-wave mixing gain versus beam ratio in BSO with moving gratings.....	31
Fig. 3.13. Measured two-wave mixing gain versus frequency detuning for different values of modulation for moving gratings.....	32
Fig. 3.14. Measured diffraction signal versus frequency detuning for different values of modulation for moving gratings.....	33
Fig. 3.15 Measured diffraction and two-wave mixing gain as a function of frequency detuning for modulation $m = 0.9$ .....	34
Fig. 3.16. Measured temporal evolution of the diffraction signal for different values of modulation depth for moving gratings.....	35
Fig. 3.17. Measured intensity gain versus beam ratio for different values of applied field strength in BTO, with ac fields.....	37
Fig. 3.18. Measured signal beam intensity versus time for different values of modulation with ac fields.....	38
Fig. 3.19. Diffraction signal in BSO versus ac field frequency for full and partial illumination conditions.....	40
Fig. 3.20. Diffraction signal in BSO versus ac field frequency for different values of intensity.....	41
Fig. 3.21. Diffraction signal in BSO versus ac field frequency for different values of applied field strength.....	42
Fig. 3.22. Diffraction signal in BSO versus ac field frequency for different values of modulation depth.....	43
Fig. 4.1. Calculated space charge field versus modulation depth for stationary recording conditions.....	46
Fig. 4.2. Measured diffraction signal versus modulation depth for stationary recording conditions.....	47
Fig. 4.3. Space charge field versus time, from the linearized theory, for stationary recording conditions with an applied electric field.....	48

Fig. 4.4. Calculated grating dynamics for different values of modulation depth, with stationary recording conditions and an applied electric field.....	49
Fig. 4.5. Measured diffraction signal versus time for modulation $m = 1$ with stationary recording conditions.....	50
Fig. 5.1. Optical absorption spectrum of ZnTe:Mn:V.....	52
Fig. 5.2. Two-wave mixing gain versus grating period at 750 nm and 1064 nm wavelengths.....	53
Fig. 5.3. Absorption spectrum of $\text{Cd}_{0.55}\text{Mn}_{0.45}\text{Te:V}$ .....	56
Fig. 5.4. Two-wave mixing gain versus grating period at 750 nm wavelength.....	57
Fig. 5.5. Two-beam coupling gain versus incident intensity for $\text{Cd}_{0.55}\text{Mn}_{0.45}\text{Te:V}$ .....	58
Fig. 5.6. Grating formation response time versus incident intensity for $\text{Cd}_{0.55}\text{Mn}_{0.45}\text{Te:V}$ .....	59
Fig. 5.7. Two-wave mixing gain versus grating period in $\text{Cd}_{0.55}\text{Mn}_{0.45}\text{Te:V}$ with an applied ac field.....	60
Fig. 5.8. Two-wave mixing gain versus ac field frequency in $\text{Cd}_{0.55}\text{Mn}_{0.45}\text{Te:V}$ .....	61

## 1. INTRODUCTION

Nonlinear optical materials allow operations in real time on the phase and amplitude of coherent laser beams. The photoinduced refractive index change in electro-optic materials, known as the photorefractive effect, exhibits unique capabilities. Dynamic holographic phase gratings can be generated in these materials with low power laser beams. The photorefractive nonlinear optical effect has many applications in optical signal processing. The first order dynamics of the photorefractive grating formation and erasure are equivalent to performing a time integration. This method of time integration is attractive for optical signal processing requiring an optically addressed spatial light modulator. Such an application exists for acousto-optic adaptive processing of radar signals.

An understanding of the photorefractive characteristics is important to the successful utilization of the nonlinear effects. The basic physical mechanisms of the photorefractive effect are well understood. Photo-generated charges are redistributed among traps, resulting in a space charge field. The material equations that describe these processes are nonlinearly coupled. Analytical solutions have been obtained through linearization in the small modulation approximation. These solutions provide an adequate description of the fundamental grating amplitude for stationary grating formations even at large modulation. However, they are not adequate in the case of nonstationary grating formation, such as moving gratings and ac fields. Numerical solutions are required in this case. Section 3 presents a detailed investigation of the nonstationary recording techniques. Numerical solutions and experimental results are presented. Section 4 presents analysis of the dynamics at large modulation.

It is desirable to perform optical signal processing at near infrared wavelengths using diode lasers. Suitable photorefractive crystals, that are sensitive at these wavelengths, have not been available. An effort to improve the performance of II-VI semiconductor photorefractives is described in Section 5.

## 2. PHOTOREFRACTIVE ACOUSTO-OPTIC ADAPTIVE PROCESSING

The photorefractive effect has applications in acousto-optic adaptive processing. In an acousto-optic correlator a signal  $s(t)$  is applied to the acoustic input of a Bragg cell, and another signal  $r(t)$  is modulated onto the laser source.[1,2] If a time integrating element is placed in the image plane of the Bragg cell, then the integrated optical exposure  $I(x)$  will contain the correlation function between  $s(t)$  and  $r(t)$ . Usually a photodetector array is used to read this exposure and extract the correlation values. Alternately, a photorefractive device could be used to perform the integration. The holographic grating that is formed in the photorefractive effect is a running time average of the light intensity pattern, characterized by the photorefractive grating time constant.[3] A photorefractive grating is read out optically, by Bragg diffraction of a readout laser beam. The phase and amplitude of the diffracted wavefront reflect the magnitude and location of the correlation.

A photorefractive acousto-optic adaptive processor which implements a least mean square algorithm to adaptively cancel radar jamming noise was demonstrated. The processor concept was developed by General Electric.[4] In their implementation a liquid crystal light valve (LCLV) was used to perform the integration function. The LCLV was identified as limiting the performance of the processor. This processor was modified to include the replacement of the LCLV with a photorefractive integrator.

The experimental layout is shown in Fig. 1.1. The acousto-optic modulator AO-1 is amplitude modulated by  $r(t)$  which is the target return signal which includes jammer noise received by the main antenna. The acousto-optic cells AO-2 and AO-3 are driven by  $s(t)$  corresponding to the signal from an auxiliary sidelobe antenna which receives a jammer noise signal that contains multiple delayed versions of the jammer noise. The algorithm finds the correlation between  $r(t)$  and  $s(t)$ , then convolves this result with  $s(t)$  to determine the signal of interest. This is the heterodyne output of the photodetector. The cancellation ability of the adaptive processor using a photorefractive crystal was demonstrated with a  $\text{Bi}_{12}\text{SiO}_{20}$  (BSO) crystal. The input signals  $r(t)$  and  $s(t)$  were

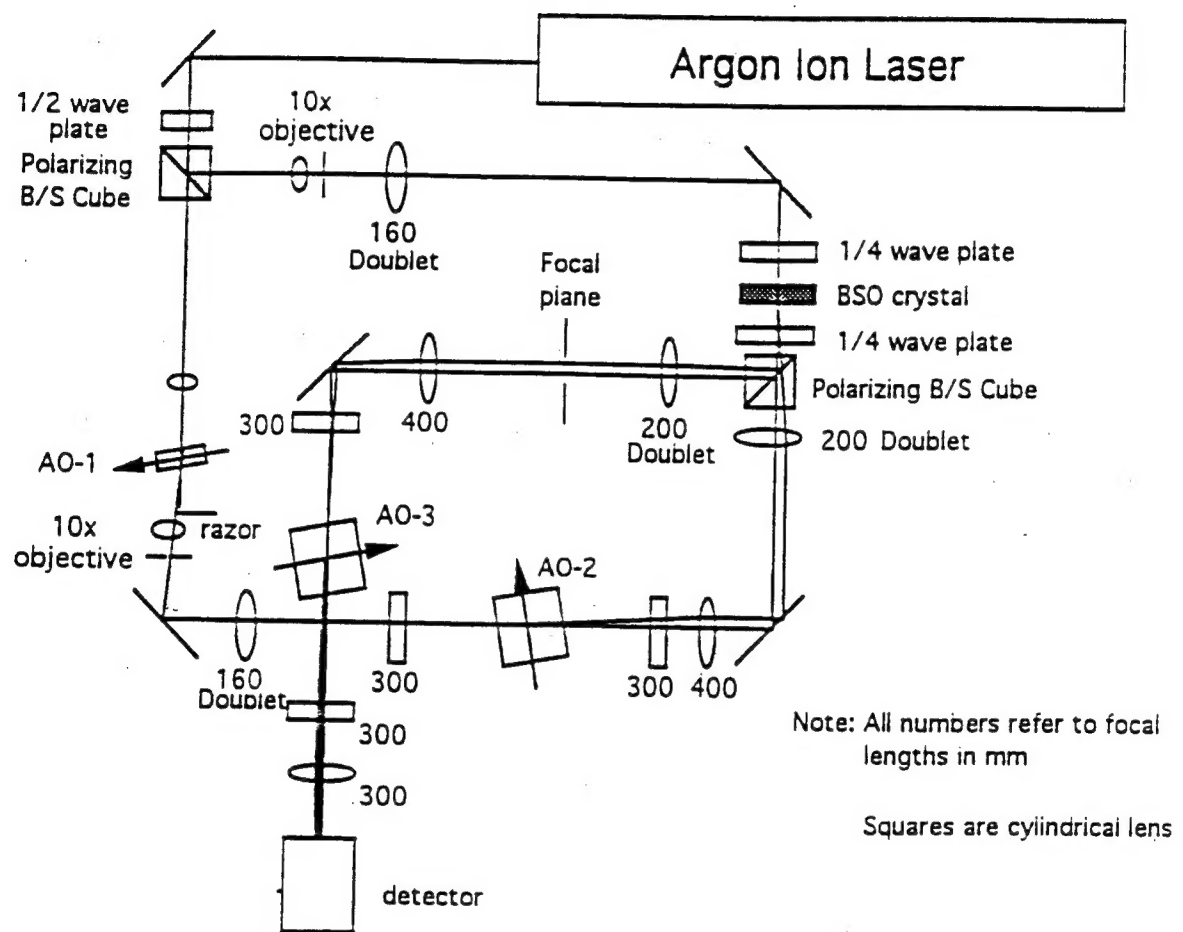


Fig. 2.1 Experimental layout for photorefractive acousto-optic adaptive processor.

---

monotone rf signals obtained from the same rf generator. A dc field of 8kV/cm was used to obtain 25 dB of cancellation.

These results demonstrate the feasibility of using a photorefractive integrator in optical signal processing. This effort did not pursue further development of the adaptive processor, as this was done elsewhere. The primary emphasis of this effort was to address the issues connected with implementation of photorefractives into optical signal processing applications. The main issues identified were diffraction efficiency, wavelength response, and speed.

Diffraction efficiency is an important concern. The diffraction efficiency of a photorefractive grating is proportional to  $(n^3 r)^2$ , where n is the index of refraction, and r is the electro-optic coefficient. It is desirable to use photorefractives with large electro-optic coefficients. These are ferroelectrics such as BaTiO<sub>3</sub>. However, the ferroelectrics have a slow response time, much slower than the 10 ms response time thought necessary for the adaptive processor application. Photorefractive crystals that are sufficiently fast include the sillenites (BSO) and semiconductors (GaAs, CdTe, ZnTe). These materials have relatively small electro-optic coefficients. Operating the device at large modulation of the intensity pattern will optimize the diffraction efficiency. However, there may be nonlinearities in the photorefractive effect which need to be understood. The photorefractive response may be enhanced by using the nonstationary recording techniques of moving gratings or ac fields.[5-7] However, significant nonlinearities in the modulation dependence have been observed.[5,8] The nonstationary recording techniques are examined in detail in section 3.

The adaptive processor described above utilized an argon-ion laser. This is not a practical laser for implementation of optical processing. The power, cooling, and size requirements of such lasers are not acceptable. Many photorefractive crystals such as BSO are sensitive to wavelengths less than 540 nm. The argon laser may be replaced by a diode-pumped, 2nd harmonic Nd:YAG laser. These lasers have recently become available at adequate powers, but are still rather expensive. It is desirable to implement optical processing with low cost, compact diode lasers. In addition the acousto-optic modulator AO-1 could be eliminated, as the diode laser could be directly modulated,

thus increasing the throughput efficiency and eliminating unwanted subbands. Unfortunately there are no suitable photorefractives with wavelength sensitivity at near infrared wavelengths. II-VI semiconductors have good figures of merit. Section 5 describes efforts to develop these devices.

### 3. NONSTATIONARY PHOTOREFRACTIVE RECORDING TECHNIQUES

Nonstationary recording techniques of moving gratings and ac fields provide the possibility of enhancing the photorefractive response in semiconductors (ZnTe, CdTe, GaAs) and sillenites ( $\text{Bi}_{12}\text{SiO}_{20}$ ,  $\text{Bi}_{12}\text{TiO}_{20}$ )[1-4]. These techniques can significantly increase the magnitude of the space charge field over that which would result from the application of a dc field alone. The increased diffraction efficiency and phase characteristics make the nonstationary recording techniques attractive for device applications. However, the large enhancements have been achieved only with weak signal beams. For modulation index  $m$  greater than about 0.02, the performance was observed to fall off significantly with increasing  $m$ .[5,8] An understanding of the nonstationary recording behavior is important when considering the limitations of these techniques.

Analytical solutions of the nonlinear material equations have been obtained by utilizing the small modulation approximation. These linearized solutions have provided good agreement with experiment for stationary recording conditions, even up to  $m \approx 1$ . For nonstationary recording conditions it is necessary to include higher harmonics when the small  $m$  approximation is not strictly valid.

Some progress was made in understanding the modulation effects with the moving grating technique.[5,9-11]. Refregier *et. al.* [5] were able to obtain partial agreement with their experimental data by applying a second order perturbation. Swinburne *et. al.* [9] and Au and Solymar[10,11] obtained numerical steady state solutions which predicted a gain saturation, but these effects were not examined in any detail.

In this section we examine the modulation dependence under nonstationary recording conditions of applied ac fields and moving gratings. A numerical capability was

developed to model the photorefractive grating formation for both ac fields and moving gratings. This is described in detail. The influence of modulation index on the magnitude, spatial distribution and temporal evolution of the space charge field is examined. Experimental results are also presented.

### 3.1 Numerical Method.

In order to determine the characteristics of the space charge field under conditions of high modulation, the grating formation was modeled with a finite difference technique. The microscopic space-charge field was calculated under the assumptions that the spatial symmetry of the grating formation was one-dimensional and periodic in the grating vector direction. With these assumptions it was only necessary to calculate the charge redistribution over one grating period of length, which was divided into N cells. The electric field, free carrier, carrier current, and charge densities were determined for each cell. The current was allowed to flow for a time period  $\delta t$  and the change in the free carrier concentration was determined by the continuity equation. The distribution of charge among free carriers and traps was then recalculated and the other quantities updated.

The material equations which describe the redistribution of charges among traps are:

$$dN_1/dt = -(S_1 I + \beta_1)N_1 + \gamma_1(N_{IT} - N_1)N_1 \quad (3.1)$$

$$dN_h/dt = -dN_1/dt \quad (3.2)$$

$$\partial N_h / \partial t = dN_h / dt - \nabla \cdot j_h \quad (3.3)$$

$$j_h = \mu_h N_h E - D \nabla N_h \quad (3.4)$$

$$\nabla \cdot E = \rho / \epsilon \epsilon_0 \quad (3.5)$$

where  $N_{IT}$  is the total number density of photorefractive centers,  $N_1$  is the number density of un-ionized charge donors,  $N_h$  is the number density of free carriers, (equations are written for positively charged carriers),  $j_h$  is the free carrier current density,  $S_1$  is the

photon absorption cross section,  $\gamma_1$  is the recombination coefficient,  $\beta_1$  is the thermal ionization rate,  $\mu_h$  is the carrier mobility, D is the diffusion coefficient given by  $D = \mu_h k_B T / q$ , E is the electric field strength which includes both the applied field  $E_A$  and the space charge field  $E_{SC}$ ,  $\epsilon$  is the dielectric constant,  $\epsilon_0$  is the permittivity of free space,  $\rho$  is the charge density, and I is the laser intensity.

The light intensity pattern is assumed to be spatially periodic with the following form:

$$I(x,t) = I_o(t) \{1 + m \sin\{Kx - \Phi(t)\}\} \quad (3.6)$$

where  $I_o$  is the total intensity, K is the grating wave number, and  $\Phi$  is the phase shift. For two vertically polarized input waves of intensities  $I_s$  and  $I_r$ ,

$$m = 2\beta^{1/2}/(\beta+1), \quad (3.7)$$

where  $\beta = I_r/I_s$ .

The distribution of charges among traps and the free carrier concentrations in each cell was determined from the rate equations, subject to the constraint of charge conservation

$$N_{li} + N_{hi} - N_{oi} = 0 \quad (3.8)$$

where I refers to the ith cell and  $N_{oi} = N_{1di} + N_{hdi} + \Delta n_{hi}$ . Here  $N_{1di}$  and  $N_{hdi}$  are the initial dark concentration levels before the light was turned on and  $\Delta n_{hi}$  is the net gain of free carriers in the ith cell due to the nonuniform current flow. A fourth order Runge Kutta technique was used to integrate the rate equations.

The photo-induced space charge field was determined by combining the one dimensional continuity equation with Poisson's equation to give

The photo-induced space charge field was determined by combining the one dimensional continuity equation with Poisson's equation to give

$$E_{SC}(x,t) = -\frac{q}{\epsilon\epsilon_0} \int_0^t j_h(x,t') dt' + G(t) \quad (3.9)$$

where  $G(t)$  is determined from the boundary condition of the constraint of a constant applied voltage.

The numerical calculations provide a temporal evolution of the space charge field. Calculations were carried out to an approximate steady state condition, typically 10-20 grating time constants. The magnitude and phase of the harmonic components were determined by Fourier decomposition of the calculated space charge field.

### 3.2 Numerical Results

The numerical method used here is very computer intensive. It was practical to calculate grating formations only for a limited, but representative set of parameters. Calculations were performed for both the moving grating and ac field techniques.

#### 3.2.1 Moving Gratings.

The moving grating technique involves the application of a dc field in combination with a frequency detuning of the laser beams.[5-7] This technique can significantly increase the magnitude of the space charge field over that which would result from the application of a dc field alone. Also the index grating is phase shifted 90°, maximizing the two-wave mixing.

In the small modulation approximation, the fundamental component of the space charge field is given by[5]

$$E_1 = i\text{m}(-E_A + iE_D)/D_1 \quad (3.10)$$

where

$$D_1 = -E_A/E_q + b(1 + E_D/E_M) + I(1 + E_D/E_q + bE_A/E_M)$$

$$E_D = Kk_B T/q, \quad E_q = qN_e/(\epsilon\epsilon_0 K), \quad E_M = \gamma_l N_e/\mu K,$$

$$b = Kv\tau_{\text{die}} \quad (3.11)$$

$v$  is the fringe velocity,  $N_e$  is the effective trap concentration, and  $\tau_{\text{die}}$  is the dielectric relaxation time. The velocity that maximizes  $\text{Im}(E_{SC})$  is given by

$$v_{\text{opt}} = A[1 + (1 - G/A^2 H)^{1/2}]/K\tau_{\text{die}} \quad (3.12)$$

where

$$A = (E_A/E_q) + E_D/E_A[1 + (E_D/E_q)], \quad B = E_M/E_D,$$

$$c = B(1 + E_D/E_q), \quad F = (E_D + E_M)E_A,$$

$$H = 1 + f^2, \quad G = 2AfB - 2Ac - c^2 - B^2. \quad (3.13)$$

The photorefractive enhancement obtained with the moving grating technique depends upon the crystal parameters, grating period, and the applied field strength, as well as the fringe velocity. In characterizing the modulation effects it is useful to define an enhancement parameter  $R$ , which is determined from the linearized theory:

$$R = E_O/(E_A + E_D) \quad (3.14)$$

where  $E_O$  is the maximum imaginary part of the fundamental component of the space charge field given by Eq. (3.10). For selenite crystals  $R$  is of the order 2-4, and can be much higher for semiconductors.

Photorefractive grating formations were calculated for parameters representative of BSO. Unless stated elsewhere, these parameters were  $\epsilon = 56$ ,  $N_E = 10^{16} \text{ cm}^{-3}$ , and  $\mu\tau = 1.25 \times 10^{-7} \text{ cm}^2/\text{V}$ , with an intensity  $I_0 = 50 \text{ mW/cm}^2$ , and an applied field  $E_A = 5 \text{ kV/cm}$ , and a  $20\mu\text{m}$  grating period. These parameters give a value of  $R = 2.6$ .

In Fig. 3.1 the calculated amplitude, imaginary component, and phase of the fundamental component of the space charge field are plotted as a function of normalized velocity  $Q = v/v_{\text{opt}}$  for various values of modulation. For small  $m$  the numerical results are in agreement with the linearized theory. At large modulation the space charge field exhibits a complicated dependence on fringe velocity. The fringe velocity that optimizes the photorefractive response is seen to depend upon modulation. For large values of  $m$  diffraction is optimized with a small nonzero fringe velocity.

The imaginary part of the space charge field is responsible for the two-beam coupling. Fig 3.2 shows  $\text{Im}(E_1)$  normalized with respect to  $m$ , as a function of beam ratio. The value of  $\text{Im}(E_1)$  plotted here corresponds to the modulation-optimized fringe velocity. According to the linearized theory,  $E_1/m$  should be constant, independent of beam ratio. Fig. 3.3 shows the same results, plotted a  $f(m)$  versus  $m$ . Here  $f(m)$  is the correction function introduced by Refregier *et al.*, [9] which relates the magnitude of the fundamental component of the space-charge field to the modulation index:

$$\text{Im}[E_1(m)] = f(m)E_0. \quad (3.15)$$

In the linear-in-modulation approximation,  $f(m) = m$ . As the numerical results show, the value of  $\text{Im}(E_1)$  increases sublinearly with  $m$ , saturating at large  $m$ . Refregier *et al.*[5] phenomenologically determined a functional form for  $f(m)$  given by

$$f(m) = 1/a[1-\exp(-am)] \quad (3.16)$$

The solid curve shown in Fig. 3.3 is a fit of this expression for  $f(m)$  to the numerical results. Other calculations were also performed for a variety of other crystal parameters and recording conditions. These calculations reflect a selection of enhancement

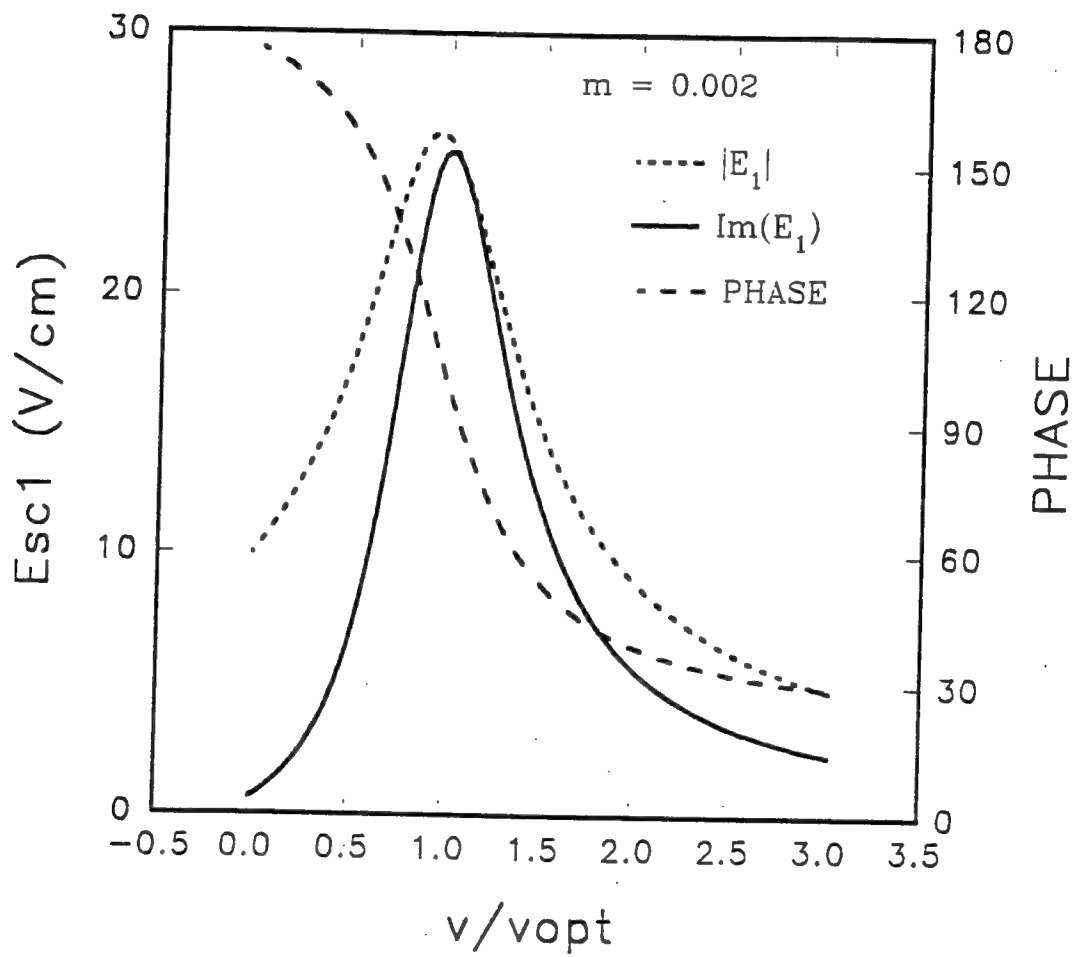


Fig. 3.1a. Calculated amplitude, imaginary component, and phase of the fundamental component of the space-charge field with moving gratings for small modulation.

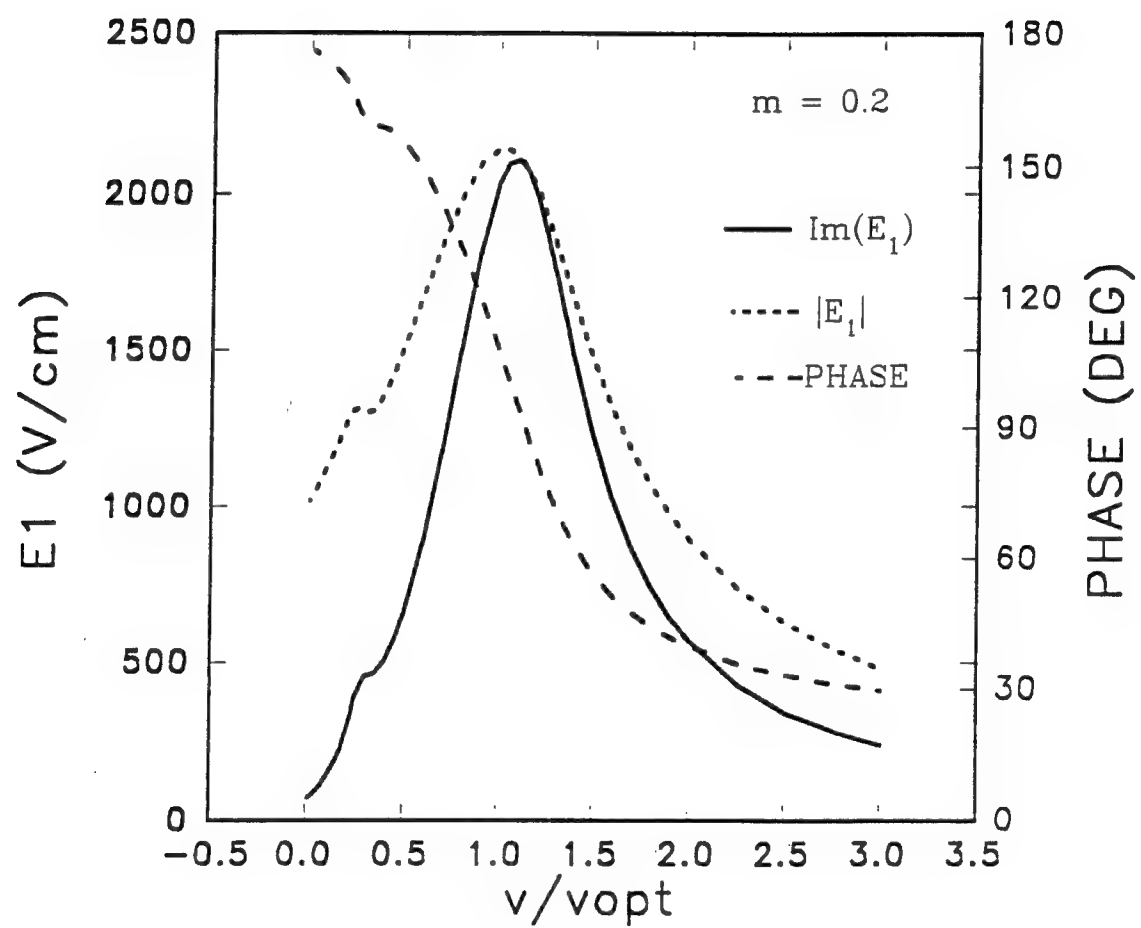


Fig. 3.1b. Calculated amplitude, imaginary component, and phase of the fundamental component of the space-charge field with moving gratings for  $m = 0.2$ .

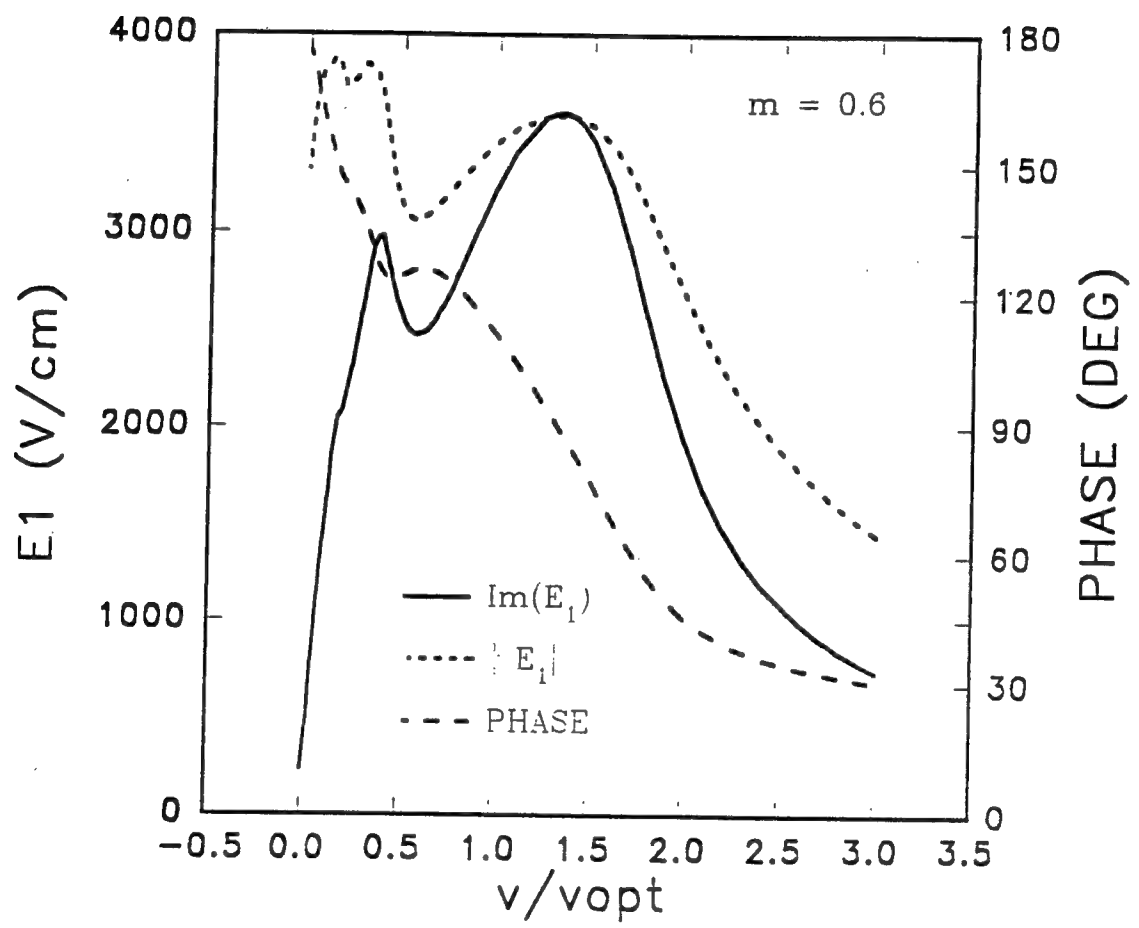


Fig. 3.1c. Calculated amplitude, imaginary component, and phase of the fundamental component of the space-charge field with moving gratings for  $m = 0.6$ .

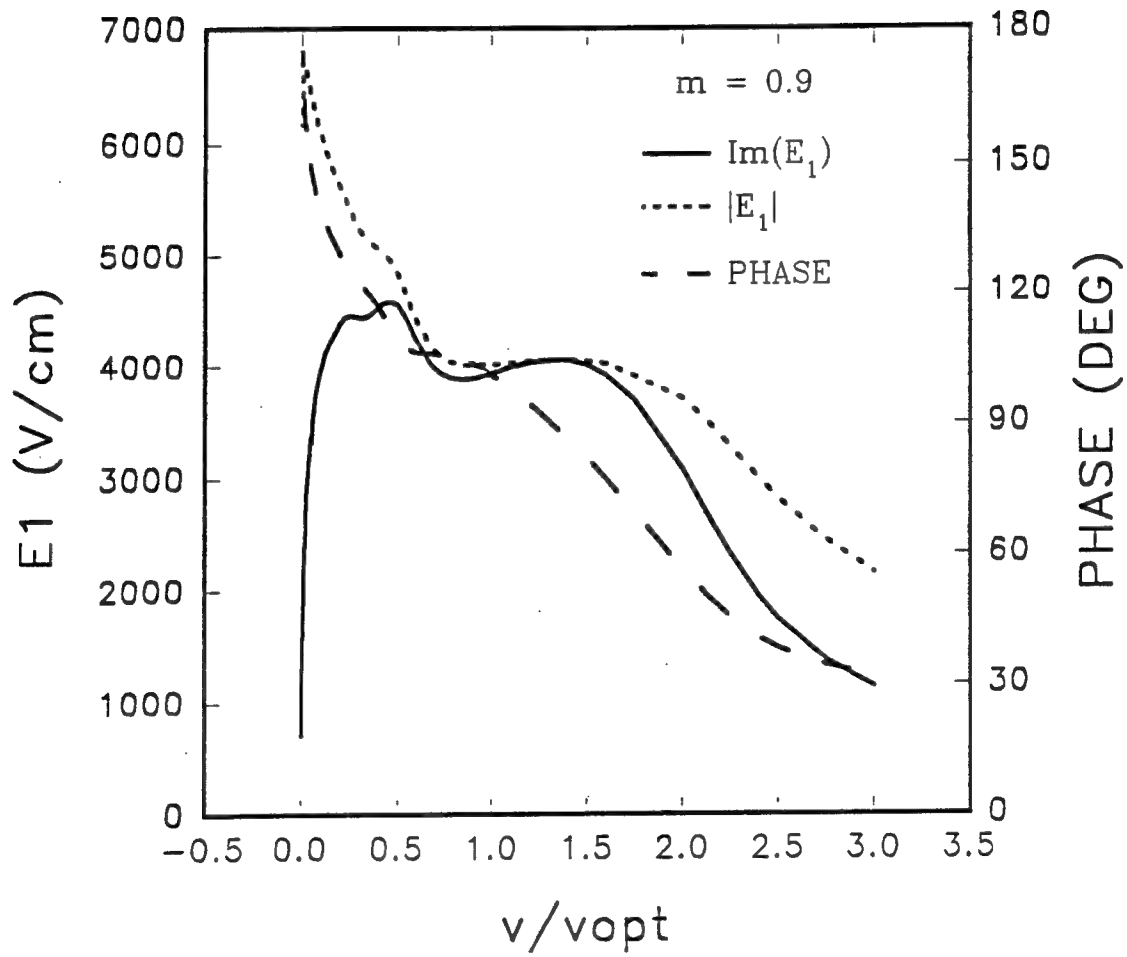


Fig. 3.1d. Calculated amplitude, imaginary component, and phase of the fundamental component of the space-charge field with moving gratings for  $m = 0.9$ .

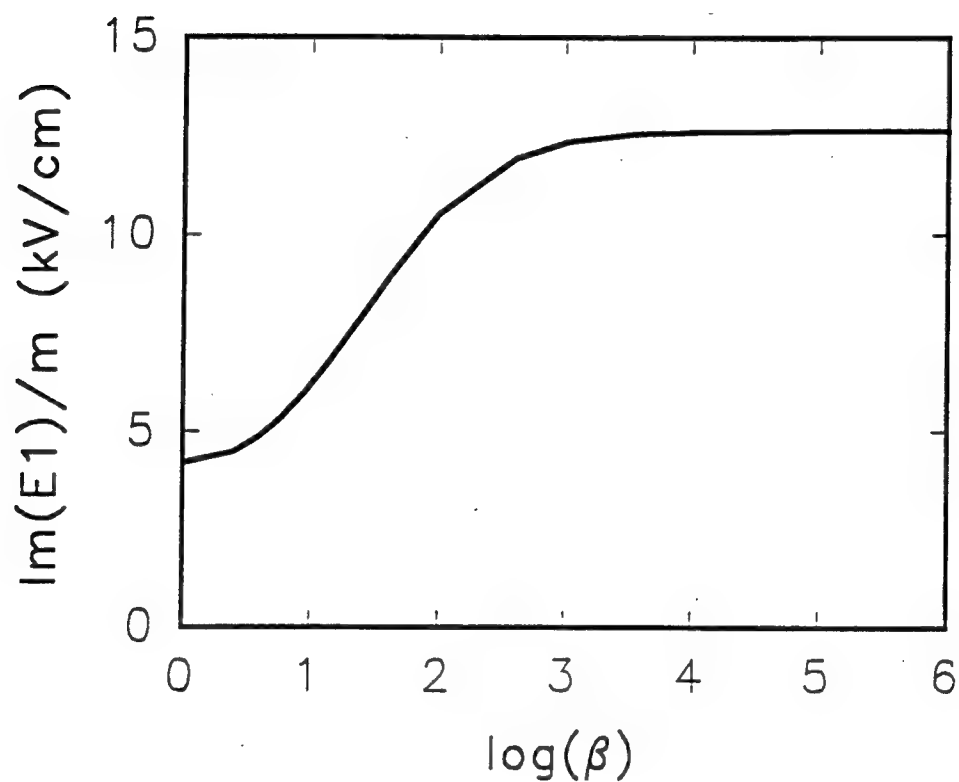


Fig. 3.2. Calculated imaginary part of the space charge field normalized with respect to  $m$  as a function of beam ratio for moving gratings.

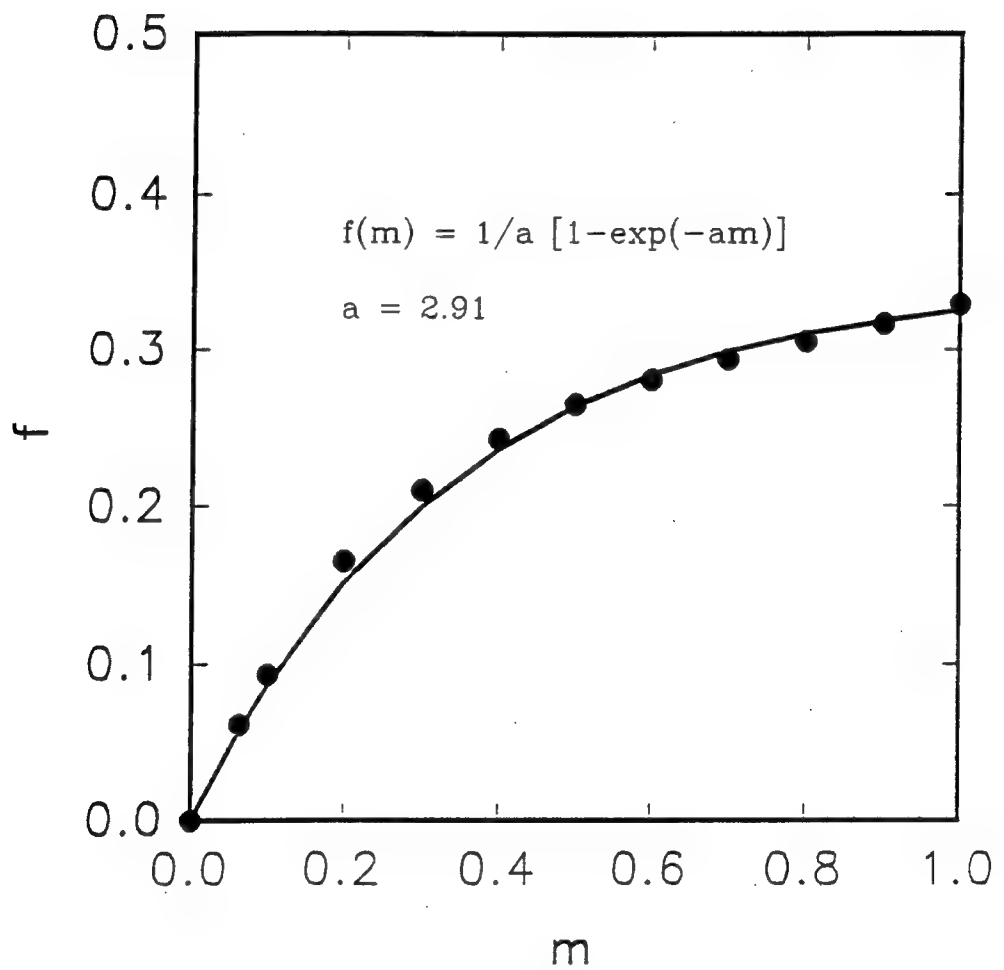


Fig. 3.3. Calculated correction function  $f(m)$ , as a function of modulation  $m$ , for moving gratings. The solid curve is a fit to equation (3.16).

conditions in which  $R$  ranged from 1 to 15. Eq. (3.16) gave a good approximation to these results. This expression for the correction function  $f(m)$  is characterized by a single parameter,  $a$ . The value of the correction parameter was found to depend linearly upon the enhancement parameter,  $R$ , as shown in Fig. 3.4. This dependence can be approximated as

$$a = 1.43R - 0.85 \quad (3.17)$$

The temporal response of the grating formation was found to also be affected by the modulation depth, as shown in Fig. 3.5. Here the magnitude of the fundamental component of the space charge field, normalized by the modulation index, is plotted for various values of  $m$  as function of the normalized time  $t/\tau_g$ , where  $\tau_g$  is the grating formation time constant determined by the linearized theory. These results correspond to grating formations at the optimum velocity for two-beam coupling. The saturation of the space charge field at large modulation gives an apparent speed increase in the grating formation. At early times  $E_1(t)/m$  is independent of  $m$ . An effective time constant  $\tau_e$  is approximately given by

$$\tau_e(m) = [f(m)/m]\tau_g. \quad (3.18)$$

This apparent speed increase applies to cases where the fringe velocity is near  $v_{opt}$ . At small velocity offsets, such as those that maximize the diffraction efficiency at large  $m$ , the temporal behavior is different. Here the grating has a long, slowly increasing tail that takes many grating time constants ( $\tau_g$ ) to reach steady state.

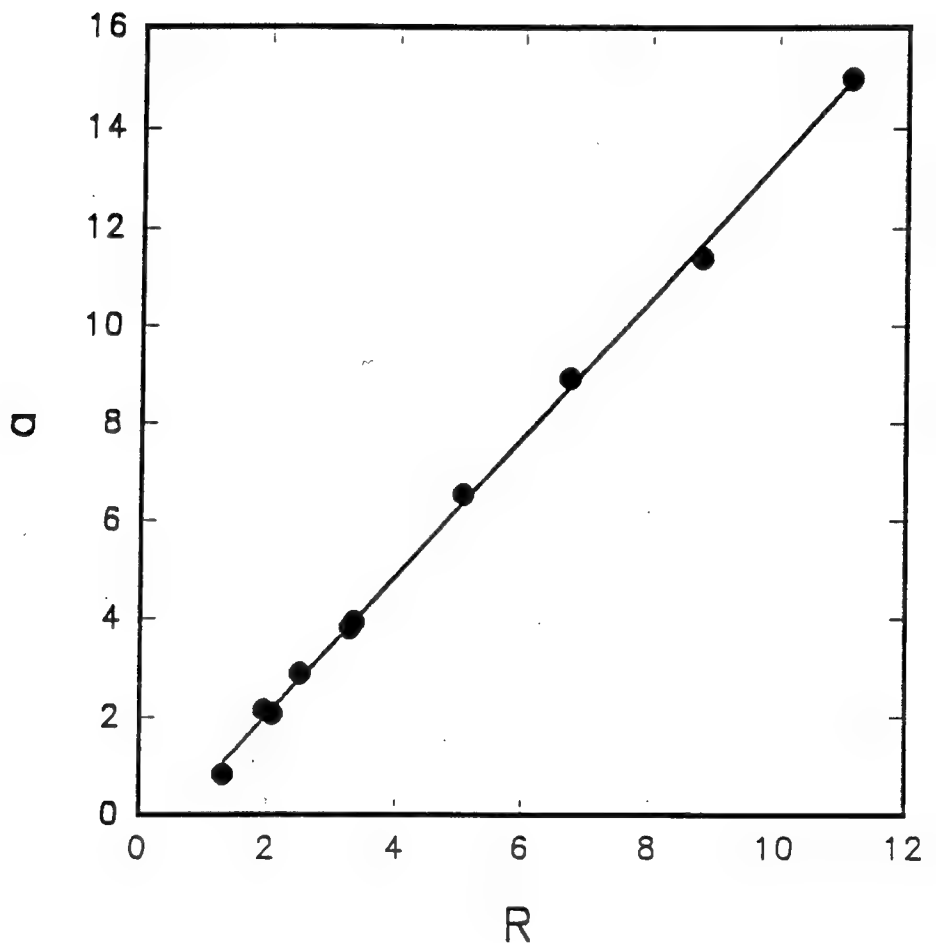


Fig. 3.4. Correction parameter as a function of the enhancement parameter for moving gratings.

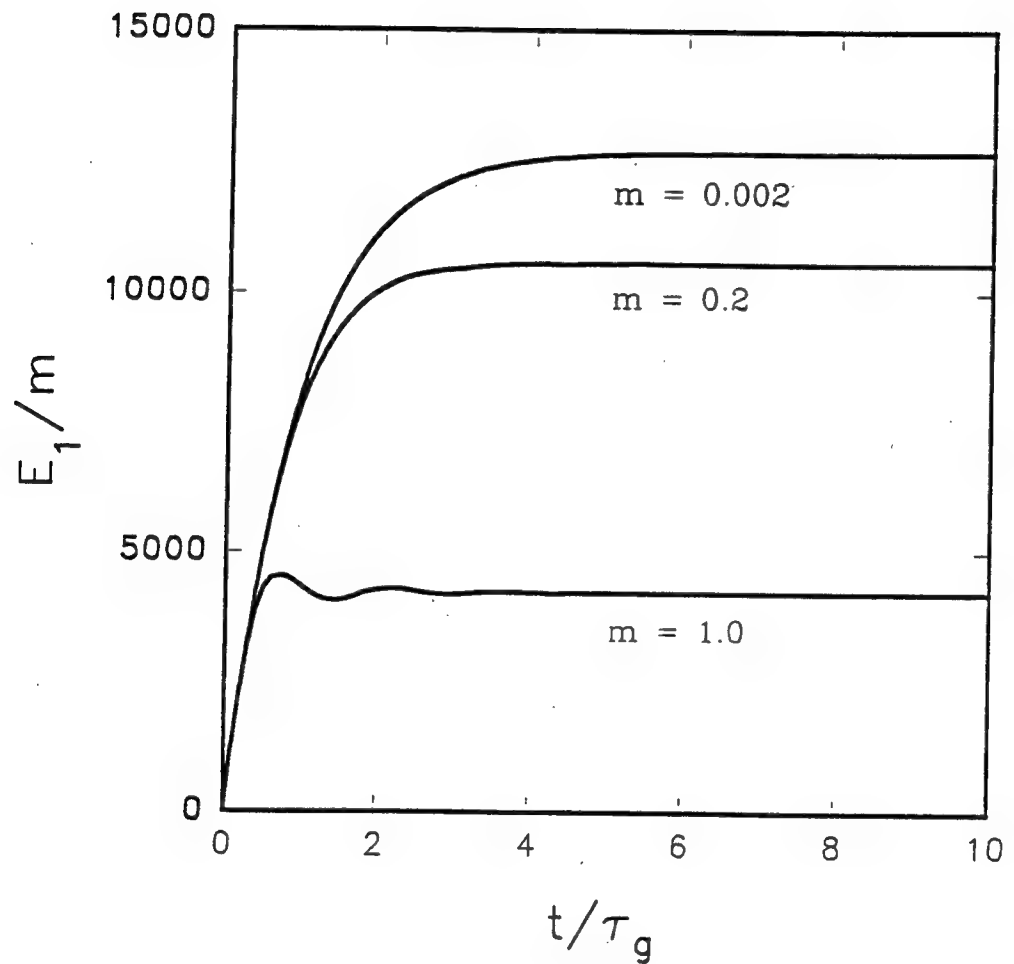


Fig. 3.5. Calculated temporal response versus normalized time for different values of modulation depth for moving gratings.

### 3.2.2 AC Fields.

#### 3.2.2.1 Modulation Dependence

In the ac field technique an external alternating square wave electric field is applied with a time period  $T_{ac}$  which satisfies the conditions  $\tau_g \gg T_{ac} \gg \tau_R$ , where  $\tau_R$  is the free carrier lifetime. The phase grating is then  $90^\circ$  phase shifted with respect to the fringe pattern, maximizing the two-beam coupling. The magnitude of the space charge field in the small  $m$  approximation is given by[6]

$$E_1 = m \frac{E_D}{(1+K^2l_S^2)} \frac{1 + KL_E E_A / [E_D(1+K^2L_D^2)]}{1 + K^2 L_E r_E / [(1+K^2L_D^2)(1+K^2l_S^2)]} \quad (3.19)$$

where  $L_E = \mu\tau_R E_A$  is the drift length,  $L_D = (D\tau_R)^{1/2}$  is the diffusion length,  $l_S = (\epsilon\epsilon_0 k_B T / q^2 N_E)^{1/2}$ , and  $r_E = \epsilon\epsilon_0 E_A / qN_E$ .

The modulation dependence of the ac field technique were calculated for BTO, with parameters  $\mu\tau = 6.8 \times 10^{-8} \text{ cm}^2/\text{V}$ ,  $N_E = 3 \times 10^{16} \text{ cm}^{-3}$ , and  $\epsilon = 47$ . These values correspond to those reported by Millerd *et al.*[6], which allows comparison with those experimental results. These results for the ac field case were similar to that of the moving grating case, in that the space charge field exhibited a sublinear dependence on modulation. The saturation value of at  $m = 1$  was  $E_1 \approx 1.2E_A$ , which was higher than for moving gratings where  $E_1 \approx 0.7E_A$  at  $m = 1$ .

The numerical results for  $E_A = 8 \text{ kV/cm}$  are plotted as  $f(m)$  vs  $m$  in Fig 3.6. It was found that the numerical results could be described quite well by the equation

$$f(m) = 1/a[1 - \exp(-am)]\exp(m). \quad (3.20)$$

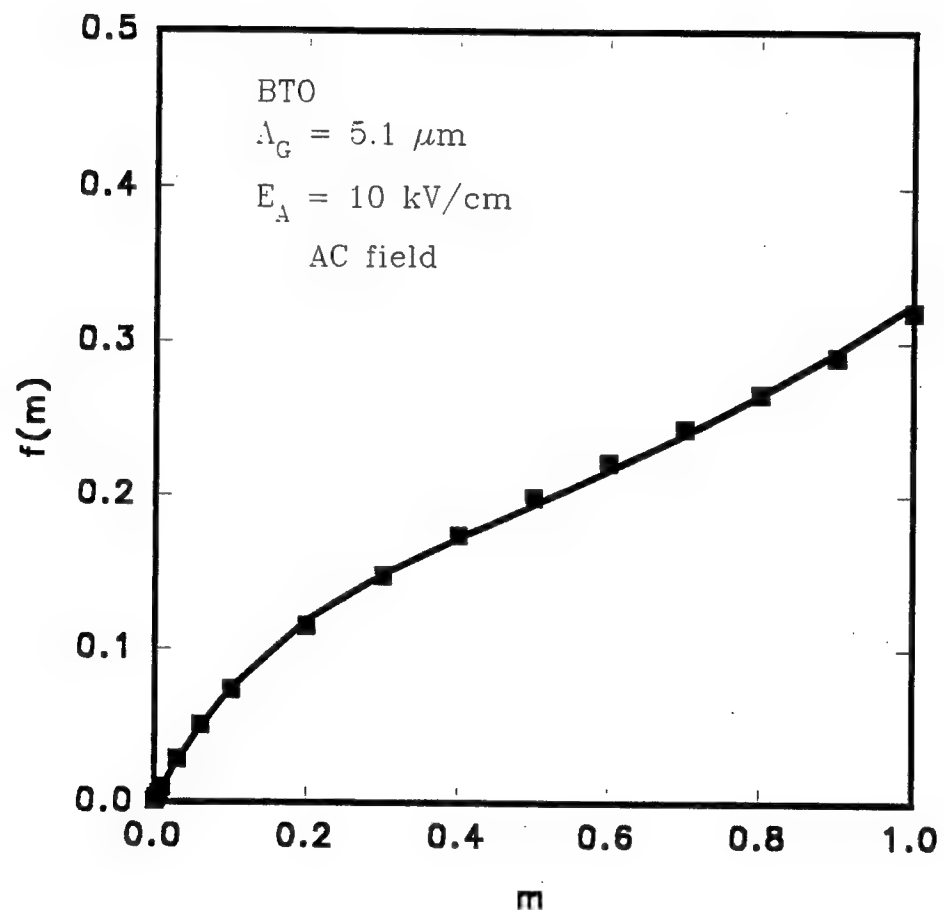


Fig. 3.6. Calculated correction function versus modulation for ac fields. The solid line is a fit of equation (3.20) to the numerical data.

As in the moving grating case, the correction parameter  $a$ , exhibited an approximately linear dependence on the enhancement parameter  $R$ , given by

$$a = 2.15R + 0.31. \quad (3.21)$$

These equations provide analytical expressions that approximate the numerical results.

The temporal behavior of the grating formation was also affected by modulation, as seen in Fig. 3.7, where the magnitude of the fundamental component of the normalized space charge field is plotted for different values of modulation as a function of normalized time,  $t/\tau_g$ . At small  $m$  the space charge field exhibits the expected exponential growth. At larger modulation the space charge field exhibits a damped oscillatory behavior. At modulation near  $m = 1$  the space charge field is "clamped" at a limiting value. The time dependence of the fundamental component of the space charge field could be written as

$$E_1(t) = f(m)E_0[1 - \exp(-t/\tau_e)\cos(\omega_e t)] \quad (3.22)$$

where  $\tau_e$  and  $\omega_e$  are functions of  $m$  and  $R$ . The value for  $\tau_e$  given by equation 3.18 agreed well with the calculated time dependence, for  $R > 1$ . The value of  $\omega_e$  depended on  $R$  and  $m$  in a complicated manner, and no analytical expression was found to describe  $\omega_e$ . At large modulation ( $m \approx 1$ ) Eq. 3.22 no longer provided a good description of the temporal behavior due to the clamping of the space charge field. It was convenient to characterize the time response by a single exponential. For the case shown in Fig. 3.7, the effective grating time constant decreased by a factor of 5 over that at small  $m$ .

For small values of  $R$  Eqs. (3.20 - 3.21) predict a superlinear behavior for  $E_1$ , consistent with the numerical calculations. The effective time constant was greater than  $\tau_g$ . In these cases the grating continued to grow over many time constants.

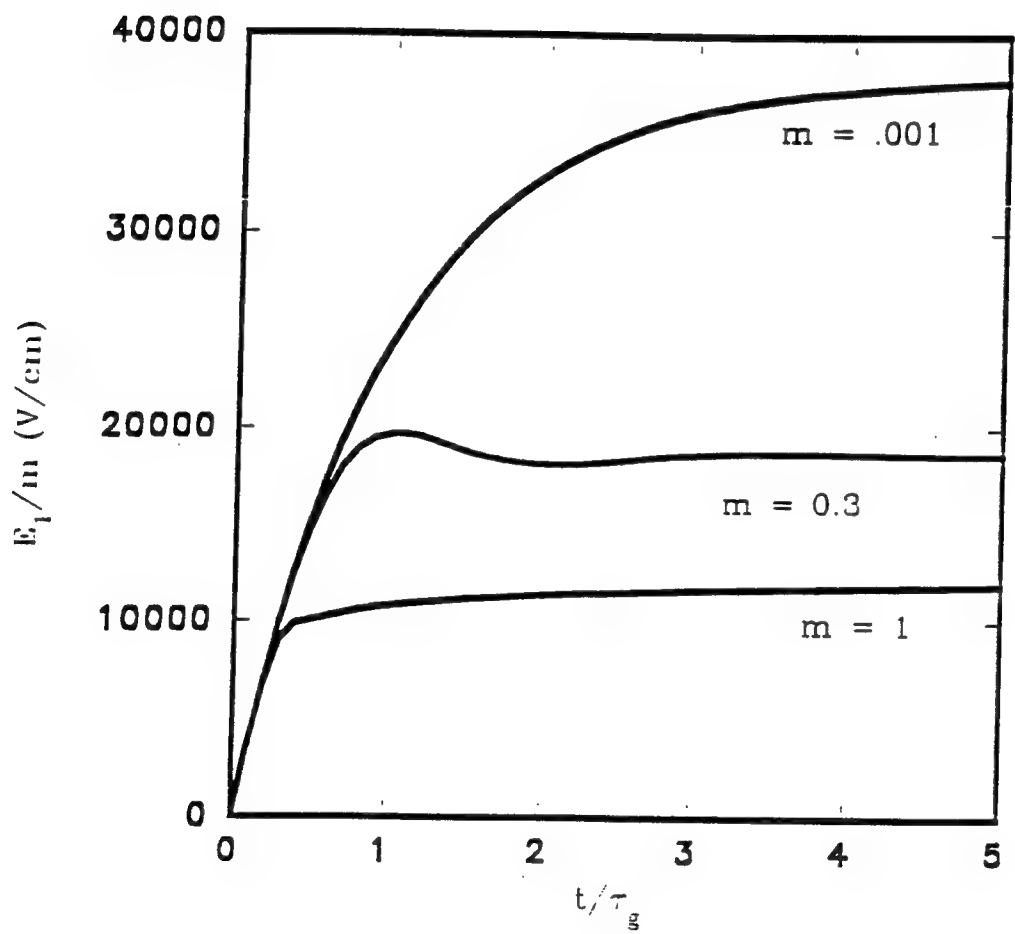


Fig. 3.7. Calculated temporal response of the space charge field for different values of modulation depth for ac fields.

### 3.2.2.2 Frequency Dependence

In the previous analysis the conditions  $\tau_g \gg T_{ac} \gg \tau_R$  were assumed to be satisfied. The results shown were time averaged. When considering the limitations of high voltage power supplies, these conditions may be difficult to meet. Temporal variations of the magnitude and phase are important considerations in signal processing. The influence of the ac field frequency on the photorefractive characteristics was also examined. For this analysis it is convenient to define a parameter  $Q = \tau_g/T_{ac}$ , which normalizes the frequency dependence.

Fig. 3.8 shows the calculated space charge field magnitude as a function of frequency for a typical BSO crystal, at low modulation. The grating time constant was chosen to be  $\tau_g = 10$  ms. Here the magnitude of the space charge field was time averaged. These results show that the optimum magnitude is expected for  $Q > 3$ .

Temporal variation in the magnitude and phase over one time period, at steady state conditions is shown in Fig. 3.9 for  $Q = 3$ . The space charge field is seen to exhibit a modulation at two times the ac field frequency. The grating phase oscillates about a 90° phase shift. For small Q these oscillations can be quite large. The magnitude of the phase fluctuation as a function of Q is shown in Fig. 3.10. For  $Q > 50$ , the phase fluctuations are less than 1%.

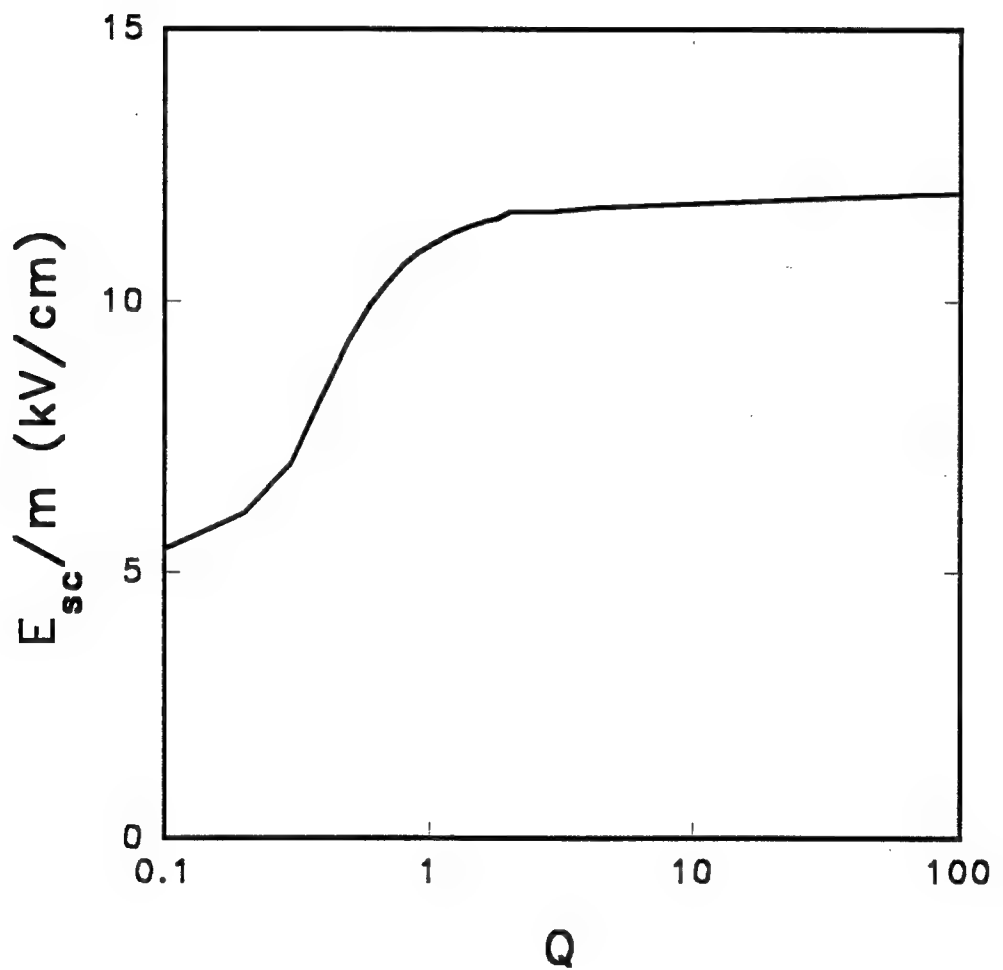


Fig. 3.8. Calculated magnitude of the space charge field versus ac frequency for ac fields.

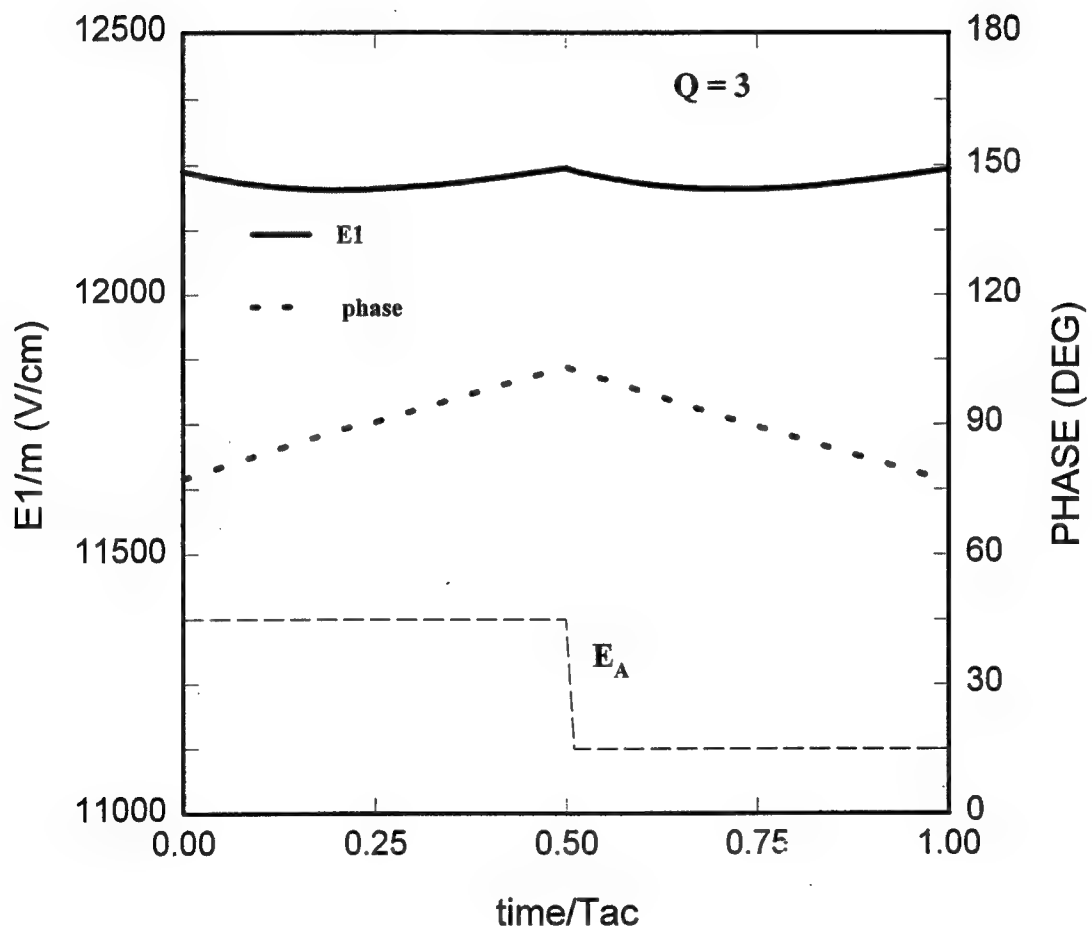


Fig. 3.9. Calculated magnitude and phase of the space charge field versus time over one period of the ac field oscillation at steady state, for  $Q = 3$ .

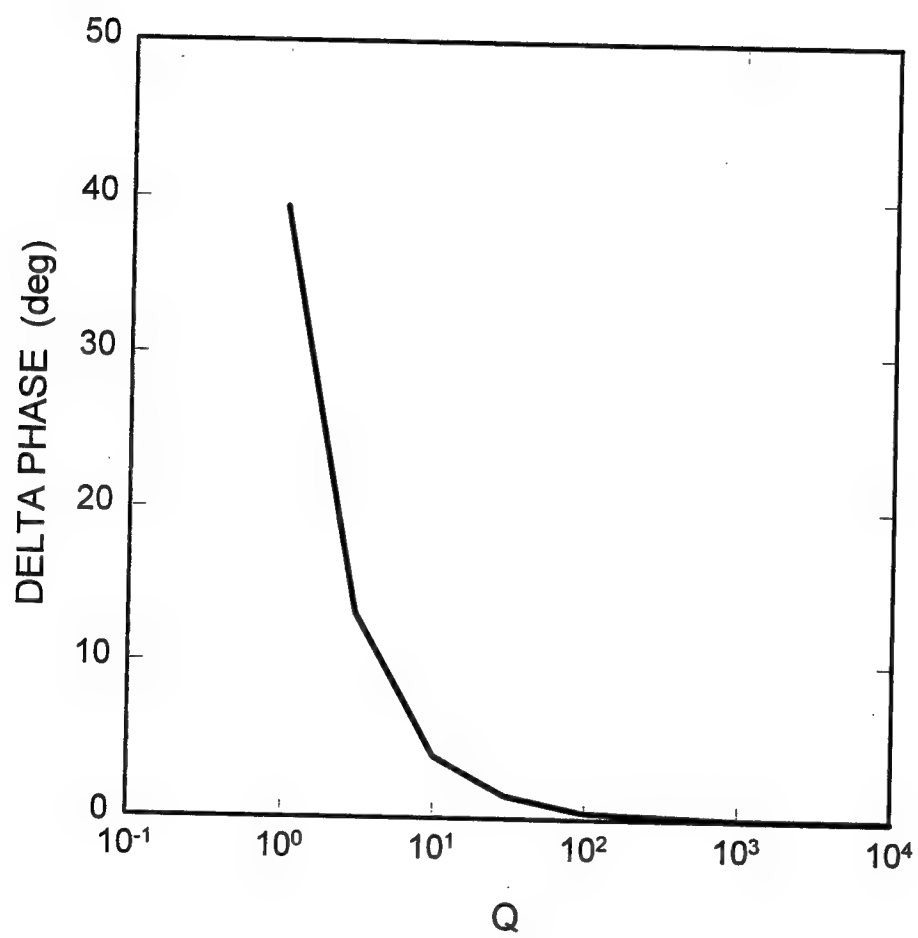


Fig. 3.10. Calculated fluctuation in phase as a function of Q for ac fields.

### 3.3 Experimental Results.

#### 3.3.1 Moving Gratings

Predictions of the numerical analysis were confirmed experimentally. The two-wave mixing gain and the grating amplitude were measured in a BSO crystal with the experimental setup shown in Fig. 3.11. The second harmonic (532nm) of a diode-pumped Nd:YAG laser was used for the experiments. Acousto-optic cells were used to produce a frequency detuning between the pump and signal beams. Each beam was frequency shifted by an acousto-optic deflector. The acousto-optic cells were driven by signal generators that were phase locked to the same temperature-stabilized crystal oscillator. Each laser beam was expanded and collimated to produce an approximately uniform illumination across the face of the crystal to reduce field screening effects. The laser beam was linearly polarized in the vertical (110) direction at the crystal entrance. The absorption coefficient was  $1.47 \text{ cm}^{-1}$  at 532 nm. The optical rotary power was 32°/mm. Polarization effects were more significant than absorption effects. An electric field was applied to the (001) crystallographic direction of the BSO crystal. This experimental configuration permitted two-beam coupling measurements and simultaneous measurement of the diffraction efficiency, which was measured with a weak He-Ne laser probe beam. The crystal had dimensions 10mm x 10 mm x 2 mm, with the 2 mm dimension in the direction of laser beam propagation. The magnitude of the electric field strength inside the crystal was determined from ellipticity induced on a He-Ne laser probe beam. An applied voltage of 7 kV across the 1 cm wide crystal resulted in a measured field strength of approximately 5.5kV.

The two-wave mixing gain was measured as a function of beam ratio for a 20- $\mu\text{m}$  grating period. The effective gain coefficient was determined according to

$$\Gamma_{\text{eff}} = (1/d)\ln[\gamma_0\beta/(\beta+1-\gamma_0)] \quad (3.23)$$

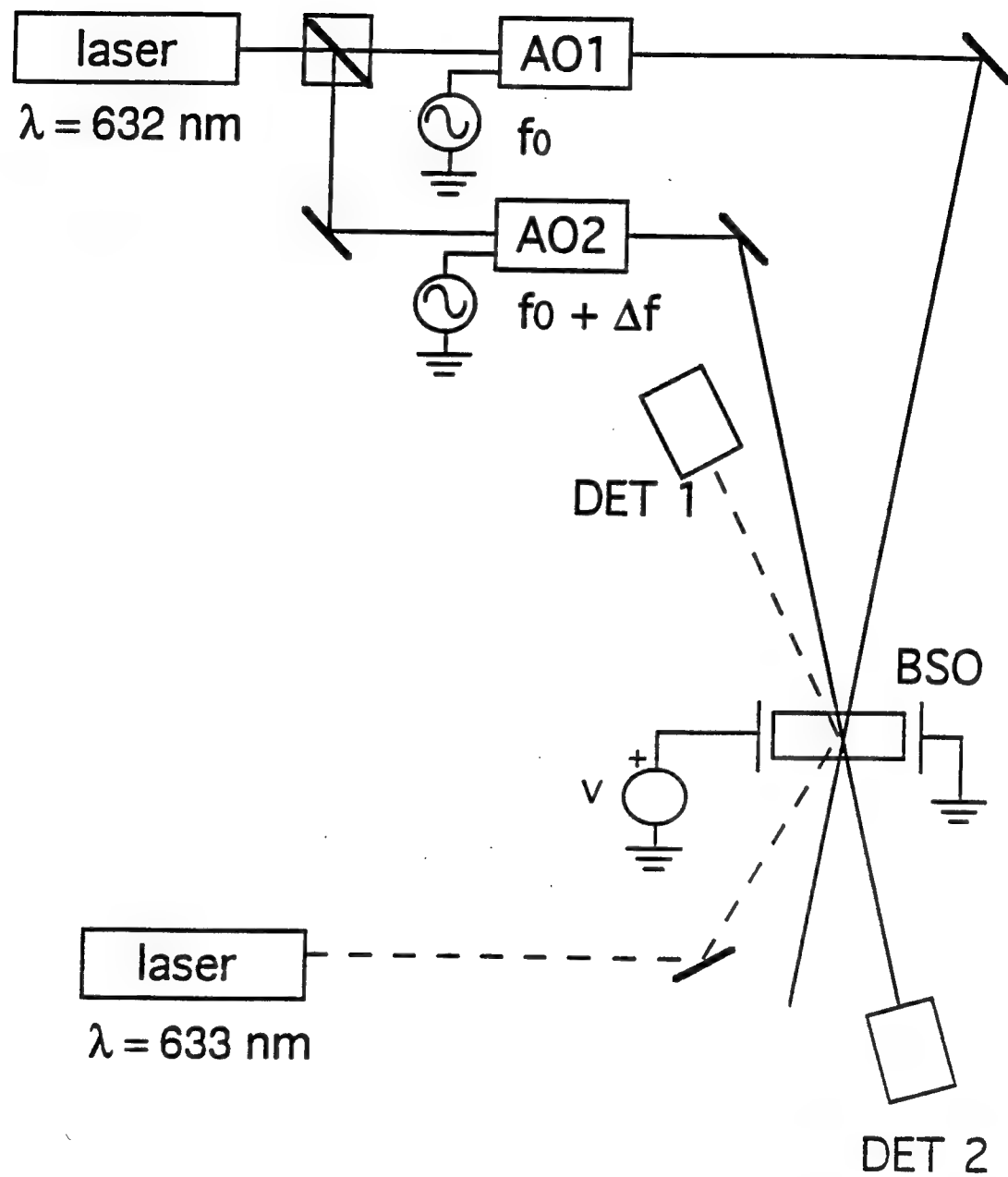


Fig. 3.11. Experimental setup for two- and four- wave mixing experiments in BSO.

where  $\gamma_0$  is the intensity gain and  $d$  is the interaction length. The results of this measurement are shown in Fig. 3.12. The gain exhibited the same fall off with small beam ratios as predicted in Fig. 3.2. The solid curve in Fig. 3.12 is a fit of the correction function  $f(m)$  given by Eq. 3.16. This fit was obtained by numerically solving the coupled wave equations that included polarization effects of optical activity and linear birefringence. The fit yielded two parameters: the small  $m$  gain coefficient  $\Gamma_s = 11.9\text{cm}^{-1}$  and the  $f(m)$  correction parameter  $a = 3.5$ . The value of  $\Gamma_s$  corresponds to the gain at the crystal entrance face. The difference between  $\Gamma_s$  and the measured small  $m$  value of  $8.43\text{ cm}^{-1}$  is due to polarization effects.

The measured fringe velocity dependence of the photorefractive response for different values of the modulation index are shown in Figs 3.13-3.15. These results are in good agreement with the predictions of Fig. 3.1. Fig. 3.13 demonstrates the shift in the optimum velocity for two-beam coupling to a higher fringe velocity with increasing modulation. The relative diffraction efficiency plotted in Fig. 3.16 is the square root of the measured diffraction signal normalized with respect to  $m$ . The normalization permits an estimate of the magnitude of the saturation effects at large  $m$ . The normalized diffraction signal at small  $m$  is approximately 5 times larger than the large  $-m$  case.

The temporal evolution of the grating for various values of modulation is shown in Fig. 3.16. Here the normalized diffraction signal is plotted for fringe velocities that optimized the two-wave mixing. The oscillatory behavior observed in the  $m = 0.02$  data is believed to be due to the heterodyning of the weak diffracted beam with scattered He-Ne light. The apparent speed increase and the clamping associated with large modulation predicted by the numerical analysis are evident. The relative grating time constants, determined by a fit of the data to an exponential time response were 1, 0.69, and 0.17 for  $m = 0.02$ ,  $m = 0.2$ , and  $m = 1$ , respectively. This compares with the prediction of 1, 0.72, and 0.27 given by Eq. 3.18, assuming a correction parameter of  $a = 3.5$ , determined by the two-wave mixing data.

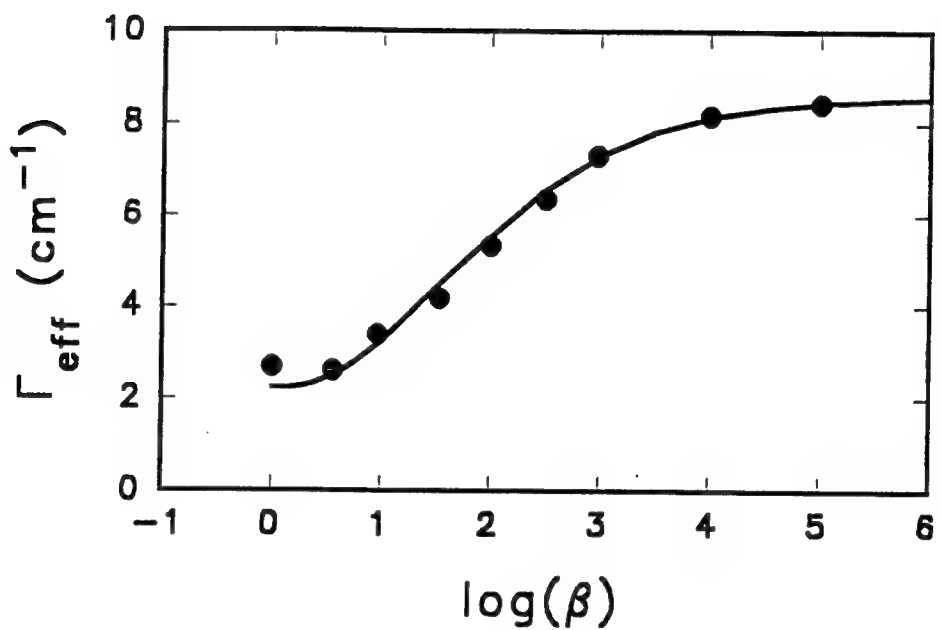


Fig. 3.12. Experimental two-wave mixing gain versus beam ratio in BSO with moving gratings. The solid curve is a fit using equation (3.16).

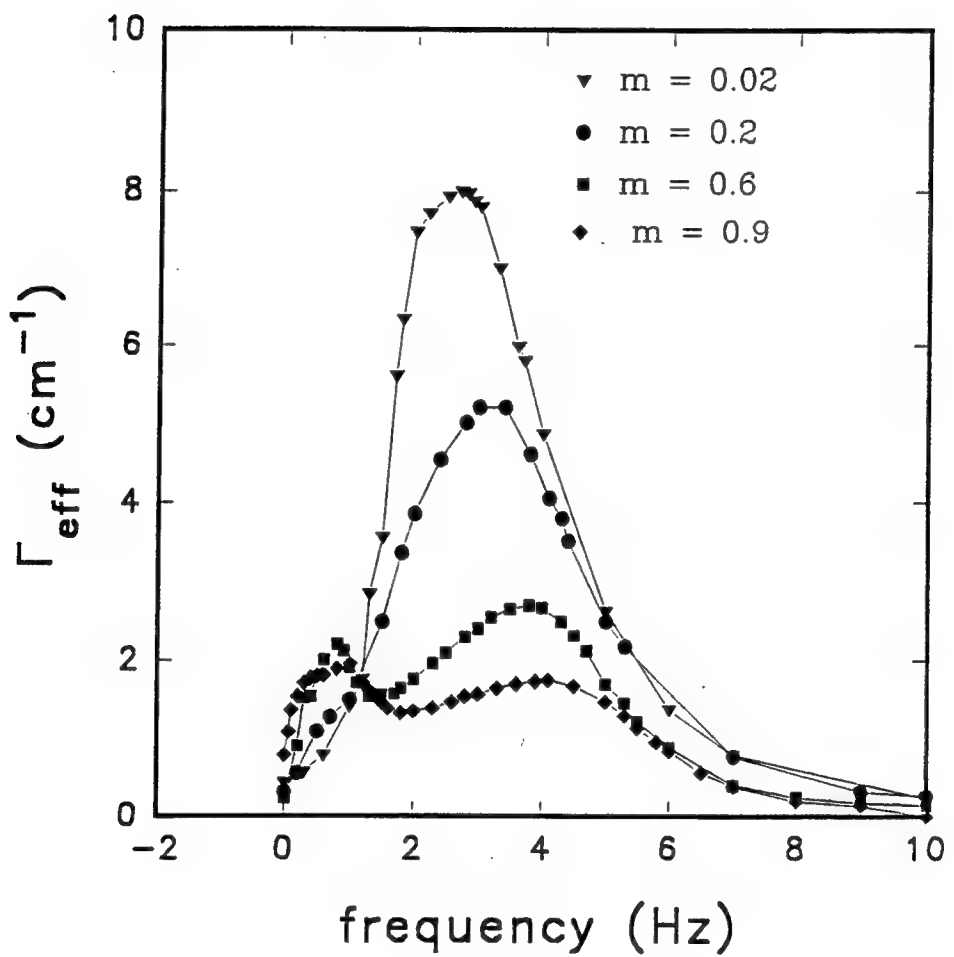


Fig. 3.13. Measured two-wave mixing gain versus frequency detuning for different values of modulation for moving gratings.

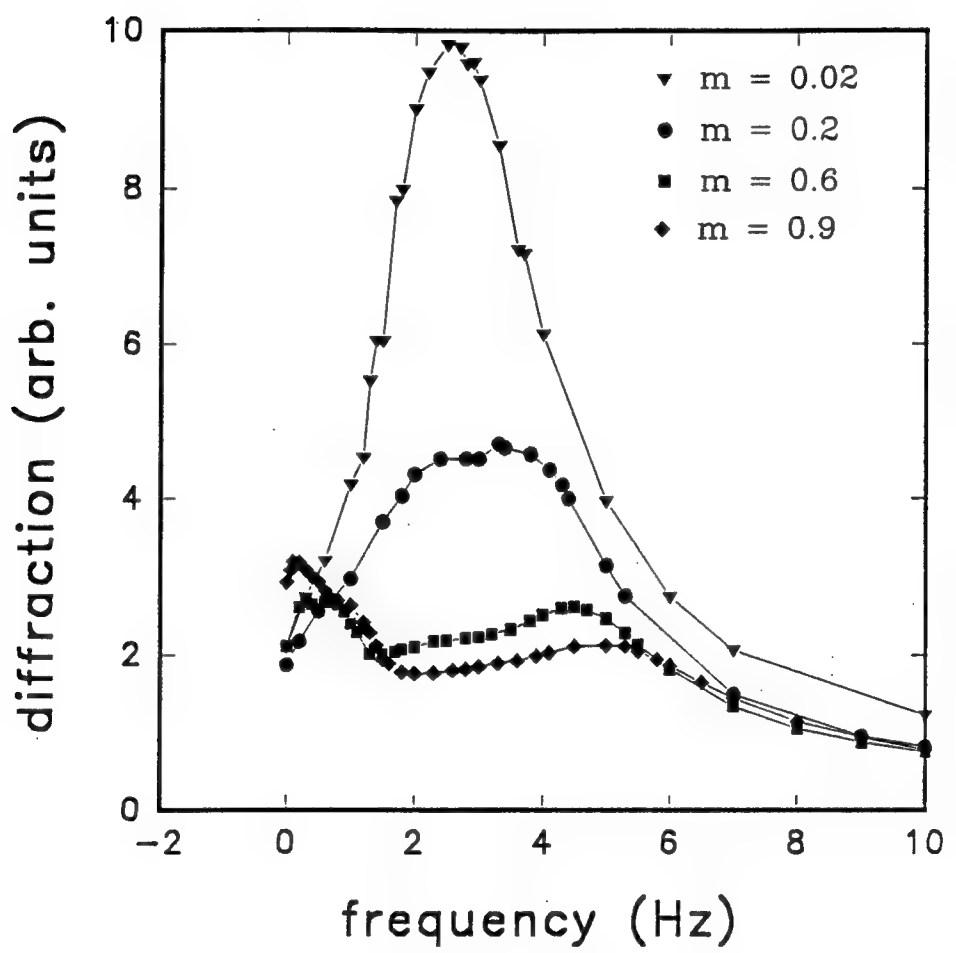


Fig. 3.14. Measured diffraction signal versus frequency detuning for different values of modulation for moving gratings.

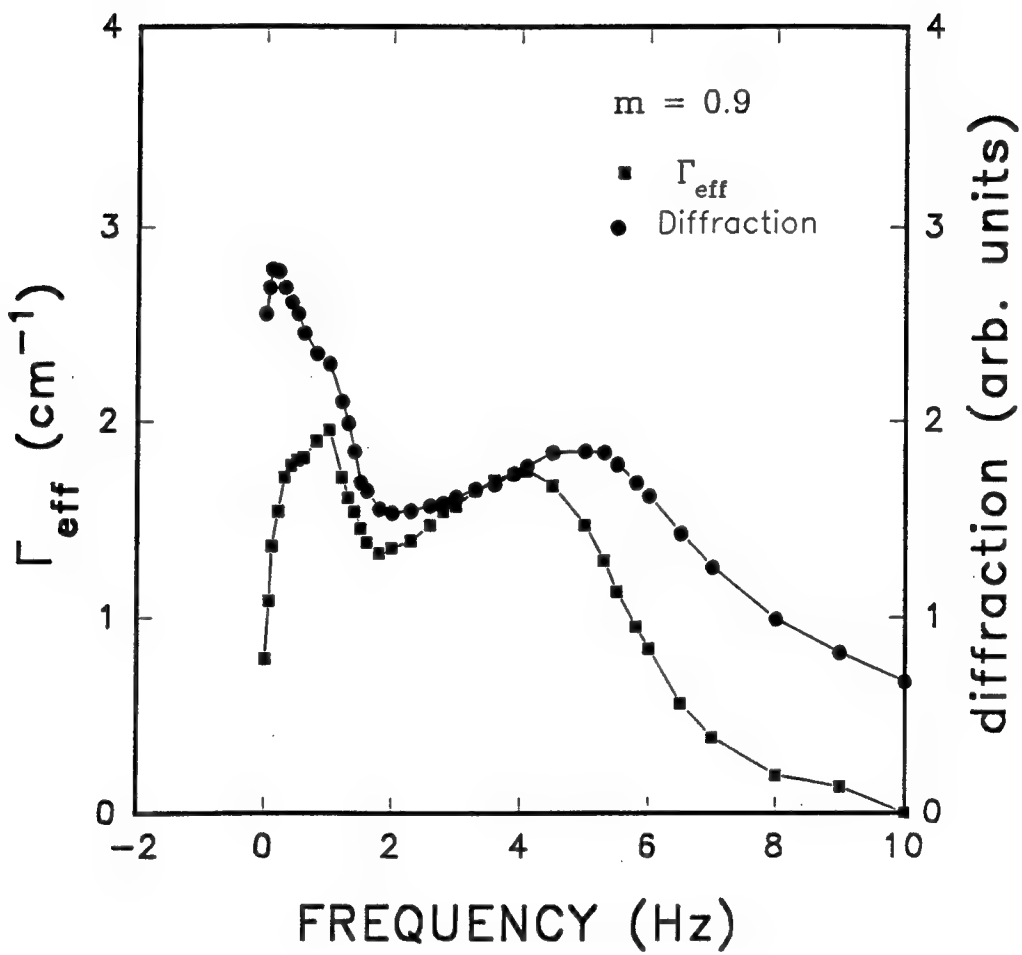


Fig. 3.15 Measured diffraction and two-wave mixing gain as a function of frequency detuning for modulation  $m = 0.9$ .

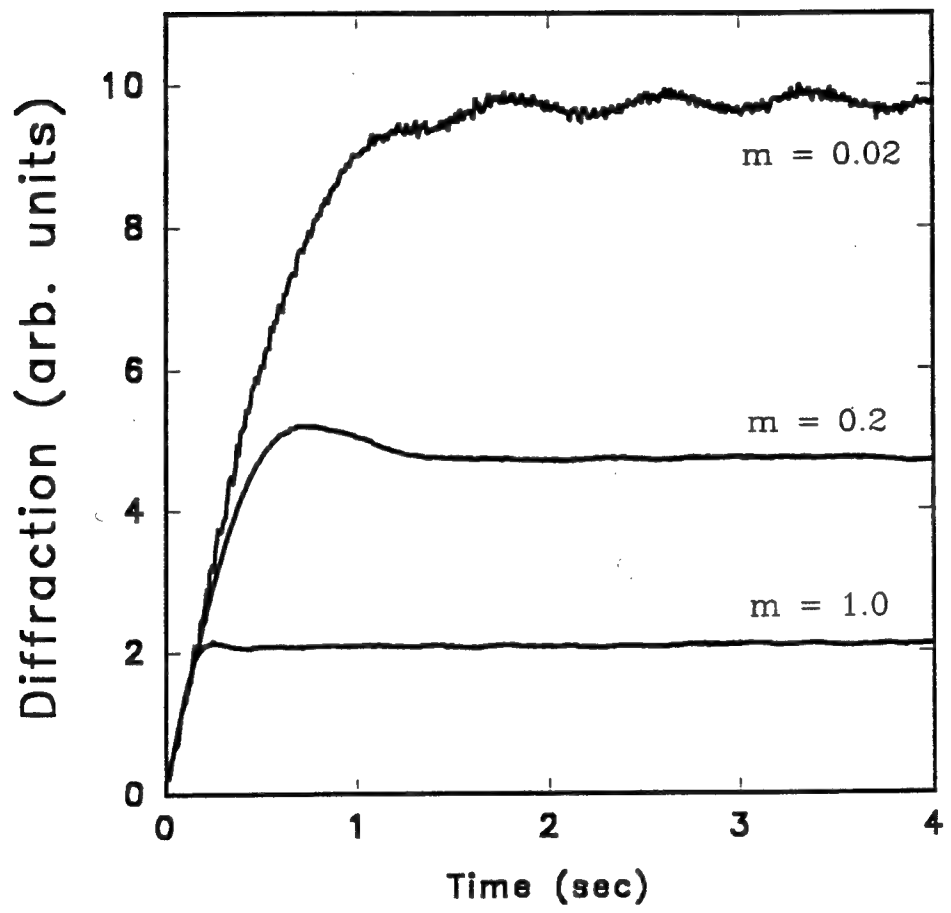


Fig. 3.16. Measured temporal evolution of the diffraction signal for different values of modulation depth for moving gratings.

### 3.3.2 AC Fields.

#### 3.3.2.1 Modulation Effects

Modulation effects with ac fields was measured in BTO. Experiments were conducted on a 1.37mm x 3.56mm x 2.74 mm (001) sample. A linearly polarized He-Ne laser at 632nm was used. The two-wave mixing gain was measured as a function of beam ratio for different applied fields. These result are shown in Fig. 3.17. The bold curves in each plot are the theoretical predictions, calculated for the measured crystal parameters of  $N_E = 3 \times 10^{16} \text{ cm}^{-3}$ ,  $\mu\tau = 6.8 \times 10^{-8} \text{ cm}^2/\text{V}$ , and  $r_{41} = 5.4 \text{ pm/V}$ . The coupled wave equations were solved numerically using the correction function calculated from these parameters. There were no free parameters. The thin line in Fig. 3.17 is the prediction of the linearized theory.

Fig. 3.18 shows the time response to the two-beam coupling process for two different beam ratios. The effective response time was decreased by a factor of 19 at large modulation.

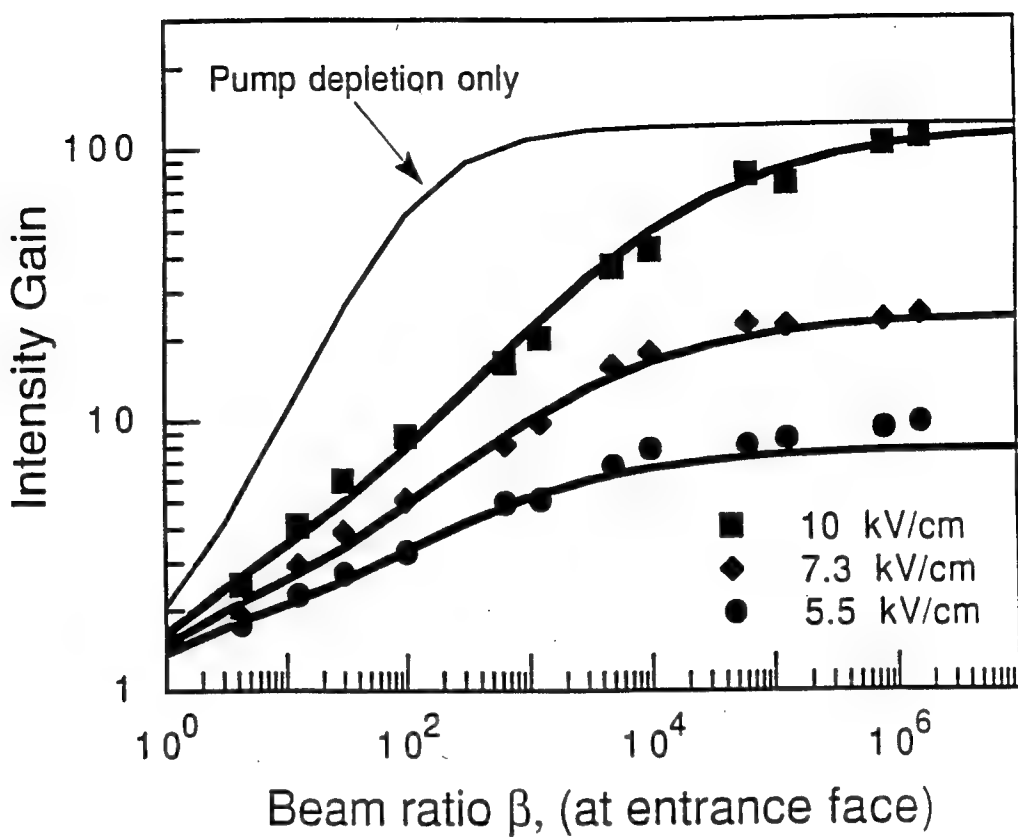


Fig. 3.17. Measured intensity gain versus beam ratio for different values of applied field strength in BTO, with ac fields. The solid lines are numerical predictions.

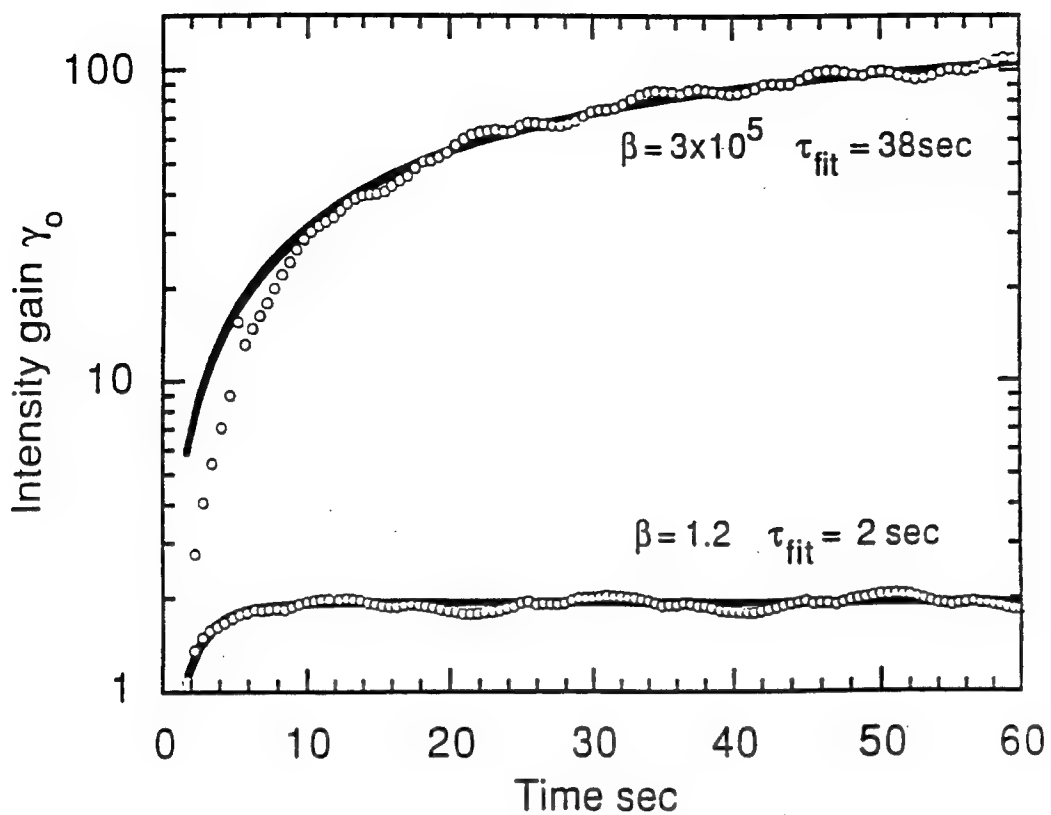


Fig. 3.18. Measured signal beam intensity versus time for different values of modulation with ac fields.

### 3.3.2.2 AC Field Frequency Dependence.

The dependence of the photorefractive response on ac field frequency was studied in BSO crystals. Experimental results are shown in Figs. 3.19-3.22. This data is for a 20  $\mu\text{m}$  grating period. Fig 3.19 shows the diffraction signal for two different illumination conditions. When the laser did not fully illuminate the crystal aperture the low frequency response was limited by field screening at frequencies less than the dielectric rate. When the laser was expanded to fully illuminate the crystal aperture, diffraction at low frequencies was observed. These results were quite different than the expected frequency response shown in Fig. 3.8. The diffraction efficiency had a large peak at low frequency, similar to a resonance. We do not believe that this is a resonance condition, but rather a fall off in the photorefractive response at the higher frequencies. The photorefractive response was also measured with the moving grating technique. These two techniques are expected to give the same response at small modulation. We found that the moving grating results corresponded to the ac field results, for frequencies near the low frequency peak. Similar characteristics were observed in six other BSO crystals tested.

The ac frequency of the peak response depended upon the applied voltage and light intensity, scaling with the photorefractive response time, as shown in Figs. 3.20 and 3.21. The peak occurred at a frequency near the grating formation rate. We observed that the magnitude of the peak had a strong dependence on modulation depth, as demonstrated in Fig. 3.22. The low frequency peak was not very evident at large modulation.

The applied field was monitored by measuring the induced birefringence on a weak test beam. No anomalous behavior was observed that could explain the frequency dependence. At the present time there is no clear explanation for the frequency dependence.

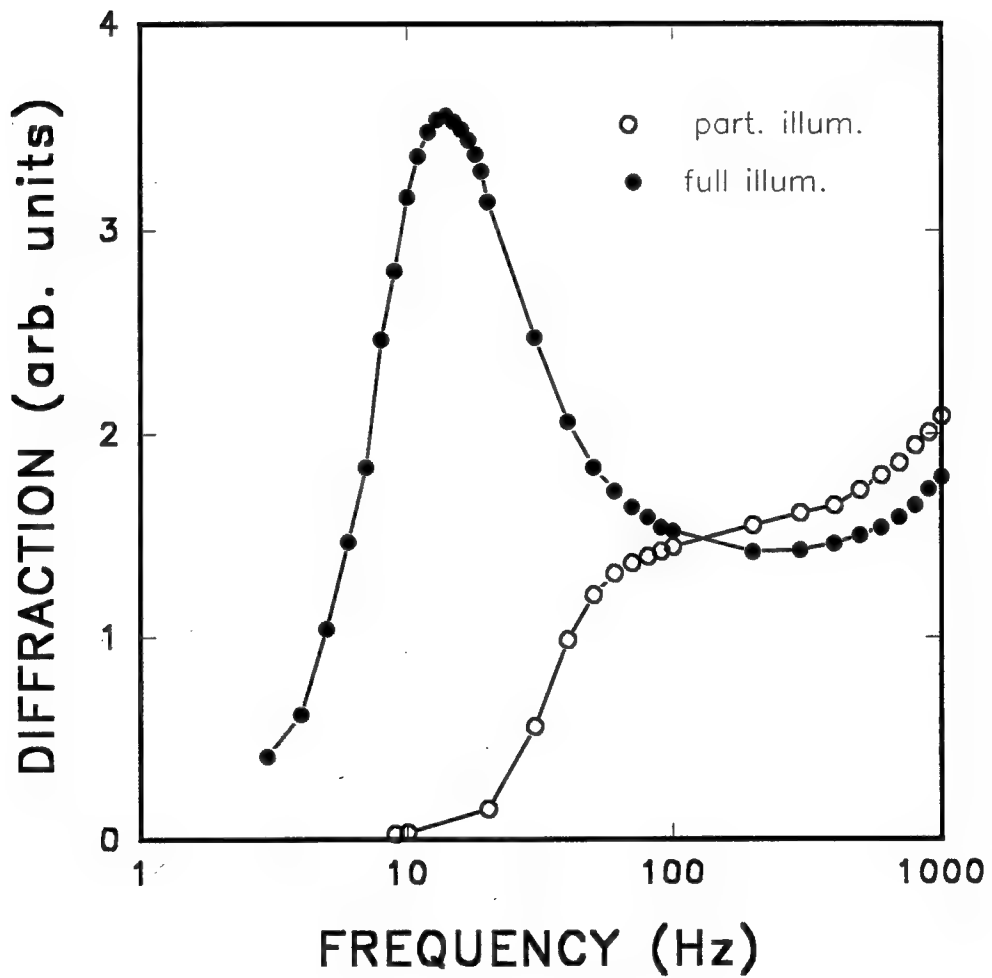


Fig. 3.19. Diffraction signal in BSO versus ac field frequency for full and partial illumination conditions.

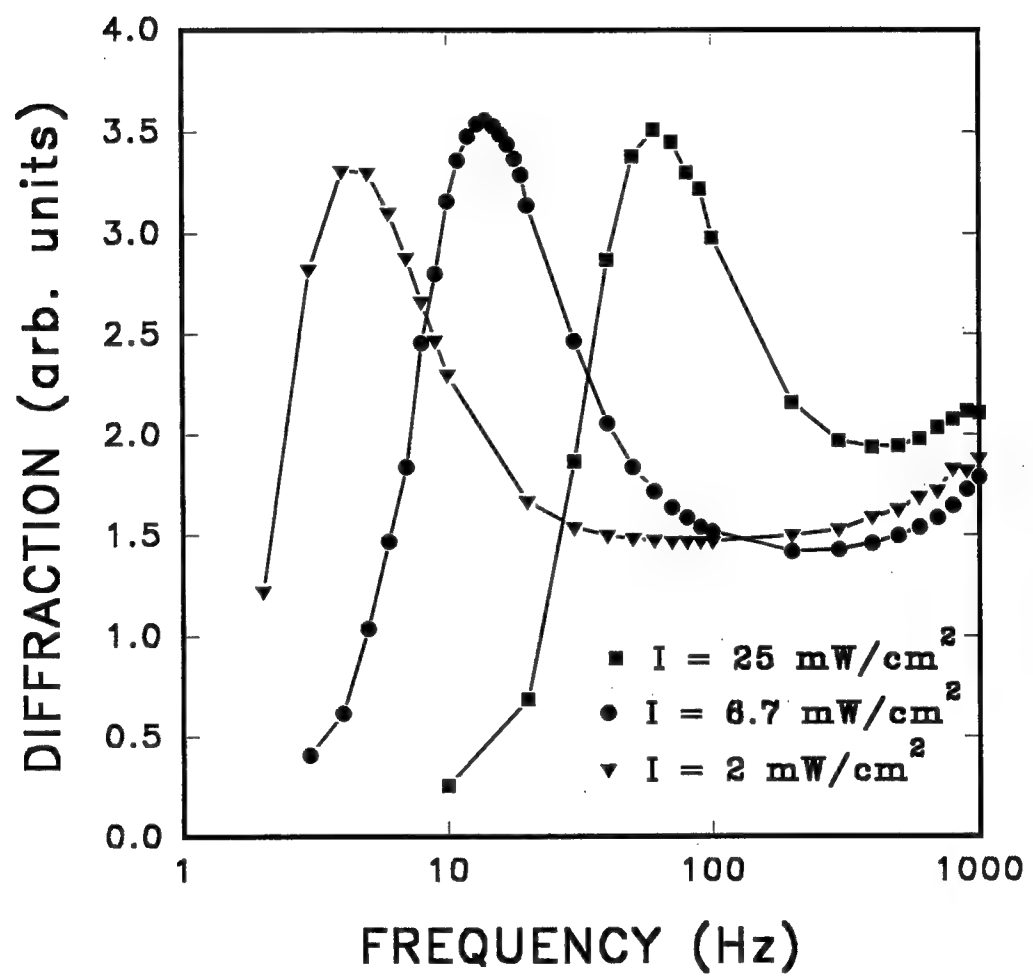


Fig. 3.20. Diffraction signal in BSO versus ac field frequency for different values of intensity.

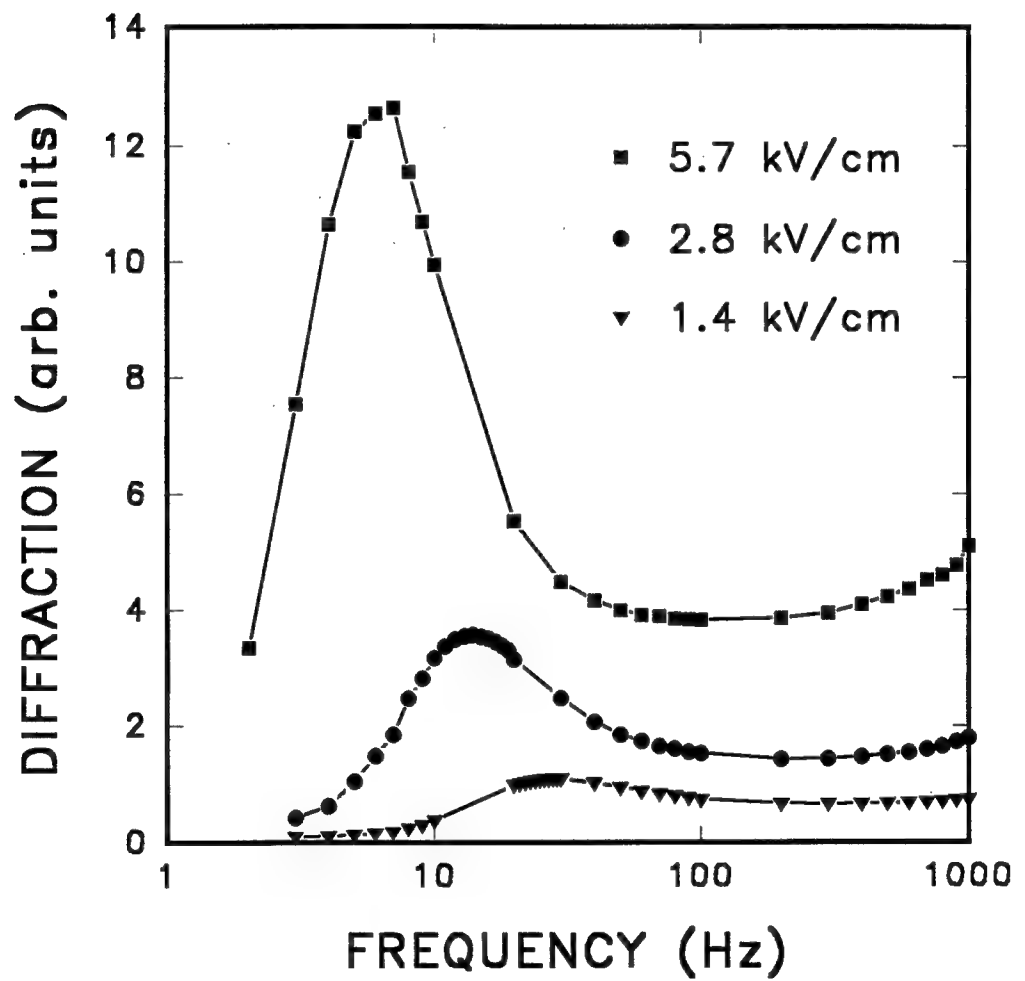


Fig. 3.21. Diffraction signal in BSO versus ac field frequency for different values of applied field strength.

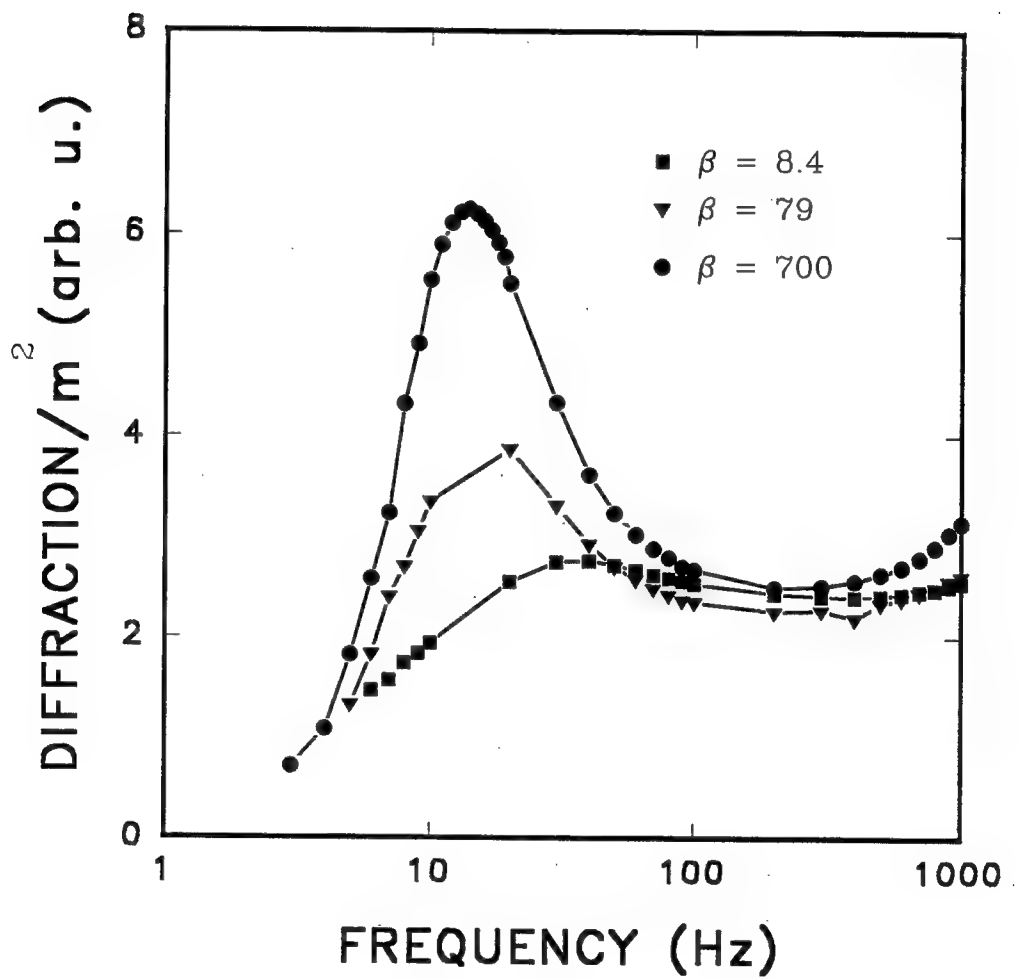


Fig. 3.22. Diffraction signal in BSO versus ac field frequency for different values of modulation depth.

### 3.4. Discussion

The nonstationary recording techniques provide the potential for enhancing the photorefractive response. However, as the results show, caution has to be used when applying these techniques to optical signal processing applications. It is desirable to operate at large modulation conditions to maximize the diffraction efficiency. The complicated phase and magnitude response of the moving grating technique show that it would not be an appropriate recording scheme to implement. The ac field technique is seen to be feasible, and in fact even desirable. Although there are large modulation effects, the photorefractive response is still optimized with the ac field technique. Phase and amplitude fluctuations can be minimized with a sufficiently fast ac field frequency. For  $Q > 100$  there is little fluctuation. This will require the availability of a good high voltage amplifier. The other advantage of the ac field technique is that it eliminates the problem of field screening, provided ac frequency is faster than the dielectric relaxation rate.

#### 4. STATIONARY RECORDING

The photorefractive response under conditions of an applied electric field and stationary recording conditions was also considered. Although the magnitude of the space charge field is less than can be achieved with nonstationary techniques, the implementation of stationary recording conditions is simpler. In this section we examine the modulation dependence for stationary conditions.

The calculated steady-state space charge field as a function of  $m$  is shown in Fig. 4.1. This corresponds to BSO with  $E_A = 5\text{kV/cm}$  and  $\Lambda = 20 \mu\text{m}$ . Similar results are obtained for other crystal parameters and conditions. The response is linear with modulation until  $m \approx 0.6$ , after which it becomes superlinear. The maximum value of the space charge field at  $m = 1$  is approximately 1.7 times the linear-in- $m$  value. Experimental confirmation of this result is shown in Fig. 4.2.

The grating formation dynamics are also affected by the modulation. Linearized solutions of the material equations predict the photorefractive space charge field dynamics can be expressed as[12]

$$E_1(x, t) = E_{10}[\cos(Kx + \phi) - \exp(-t / \tau_g) \cos(Kx + \phi + i\omega_g t)]. \quad (4.1)$$

Equation 4.1 shows that the space charge field has a damped oscillatory response with a time dependent phase. This behavior is shown in Fig. 4.3. Calculated grating dynamics for different values of modulation are shown in Fig. 4.4. This result shows that for  $m$  greater than about 0.2 the grating dynamics are no longer accurately described by the damped oscillatory behavior of Eq. (4.1). For very large modulation,  $m \approx 1$ , a very long time is required to reach the steady state. This was verified experimentally, as shown in Fig. 4.5.

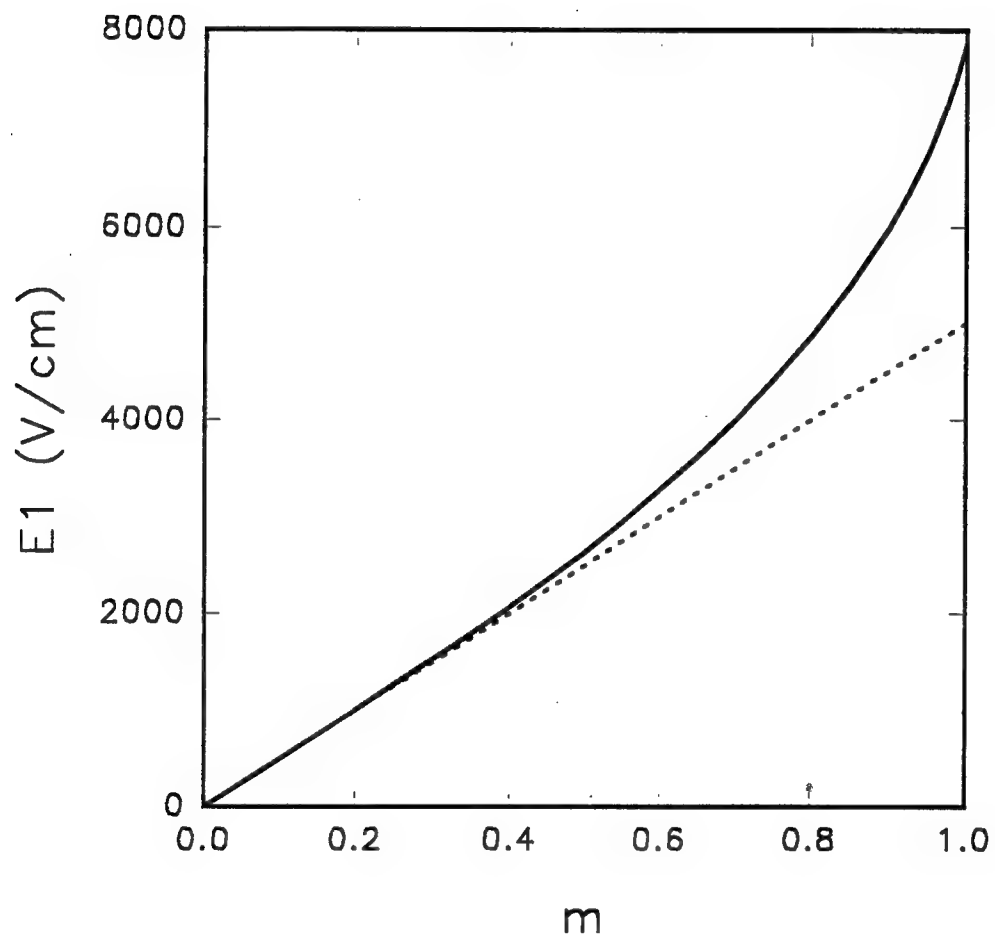


Fig. 4.1. Calculated space charge field versus modulation depth for stationary recording conditions.

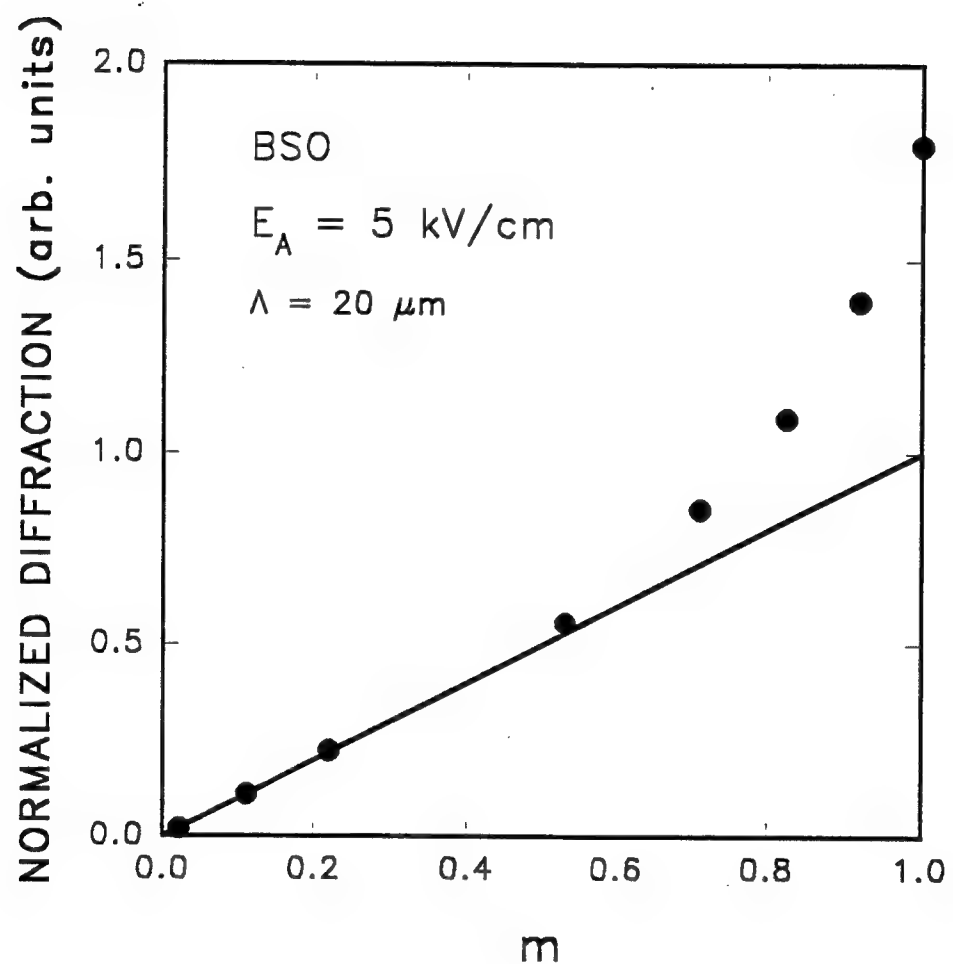


Fig. 4.2. Measured diffraction signal versus modulation depth for stationary recording conditions.

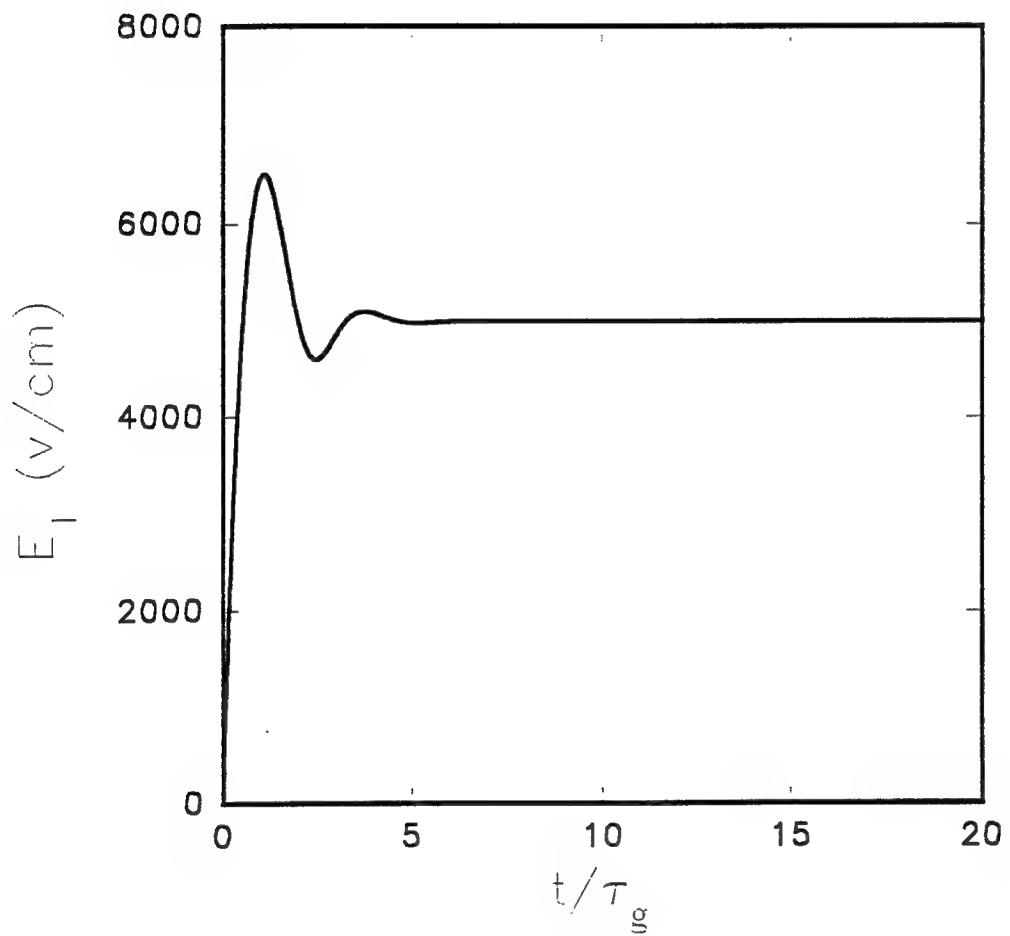


Fig. 4.3. Space charge field versus time, from the linearized theory, for stationary recording conditions with an applied electric field.

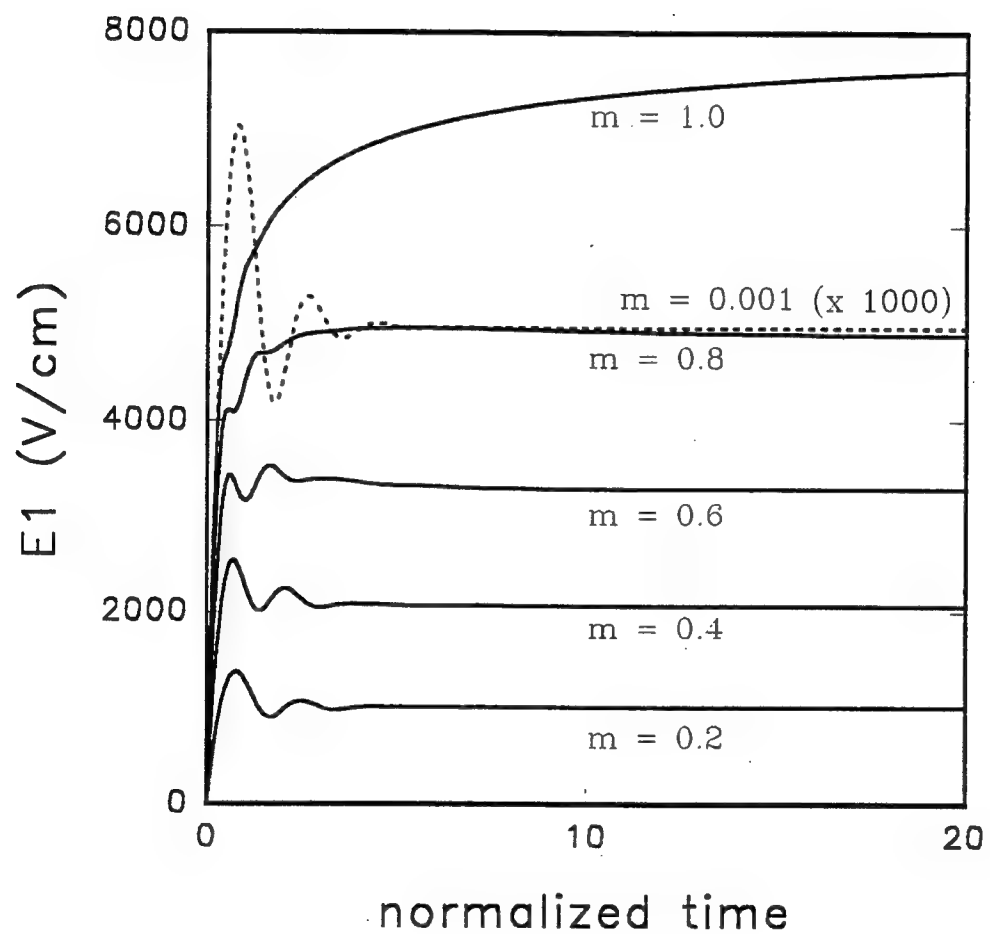


Fig. 4.4. Calculated grating dynamics for different values of modulation depth, with stationary recording conditions and an applied electric field.

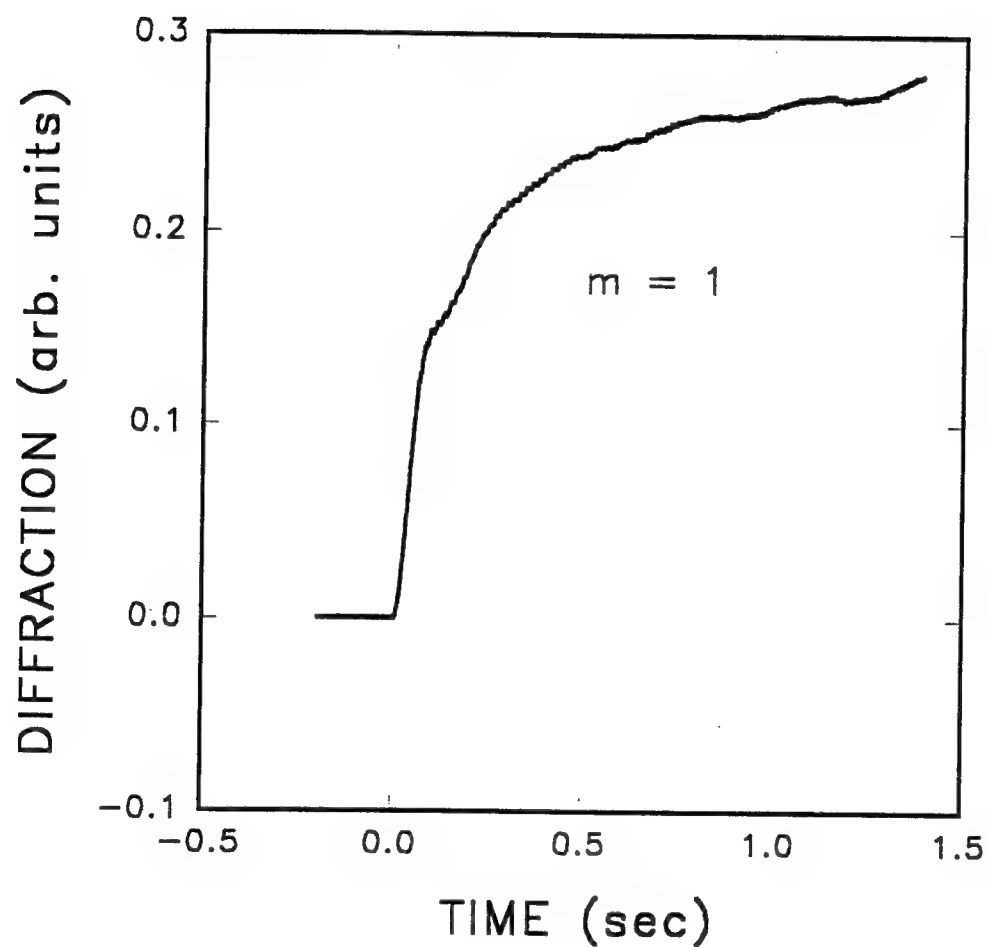


Fig. 4.5. Measured diffraction signal versus time for modulation  $m = 1$  with stationary recording conditions.

## 5. II-VI PHOTOREFRACTIVES.

II-VI semiconductors have good potential for use in real time optical signal processing. They have the best figures of merit of the semiconductor photorefractories, with wavelength sensitivity in the near IR. Efforts were initiated to investigate and develop these photorefractories. The ZnTe and CdTe crystals investigated in this effort were grown at Brimrose Corp. of America.

### 5.1 ZnTe

Photorefractivity had been demonstrated in ZnTe:V[13], which has wavelength sensitivity from 0.6 to 1.5  $\mu\text{m}$ . In that earlier work it was found that incorporation of vanadium in ZnTe was very difficult. Even when vanadium was incorporated as an active impurity the doping usually was not uniform, and the response was limited by the effective trap concentration of  $N_e \approx 10^{14} \text{ cm}^{-3}$ , which is much lower than typical values of  $N_e \approx 10^{15} - 10^{16} \text{ cm}^{-3}$ . In an effort to incorporate more traps, ZnTe co-doped with V and Mn was grown and characterized.

The ZnTe:V:Mn crystals were grown from vapor phase by Physical Vapor Transport. The starting concentrations of vanadium and manganese in the compound material were  $5 \times 10^{19} \text{ atoms/cm}^3$ . All of the grown crystals were p-type with resistivity in the range of  $5 \times 10^8 - 10^{10} \text{ ohm-cm}$ . A typical optical absorption spectrum is shown in Fig. 5.1. Electron paramagnetic resonance (EPR) spectroscopy showed a strong Mn signal, indicating that Mn was incorporated into the lattice. Optical EPR measurements were performed with light at 514nm, 619nm, 727nm, and 800nm. The detected EPR signal decreased under illumination, indicating that the density of  $\text{Mn}^{2+}$  species decreases upon illumination. These observations signify that the Mn co-dopant is optically active and therefore affects the optical and photorefractive properties. Photorefractive characterization of the ZnTe:V:Mn samples were performed by two-wave

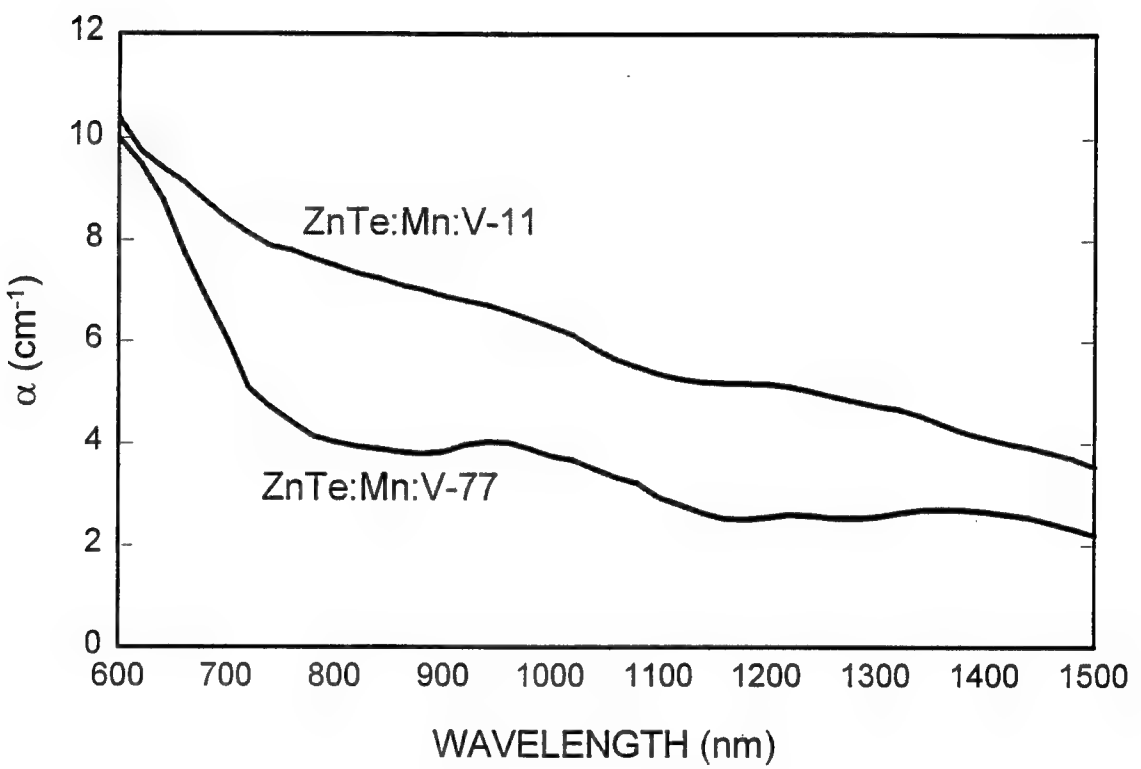


Fig. 5.1. Optical absorption spectrum of ZnTe:Mn:V.

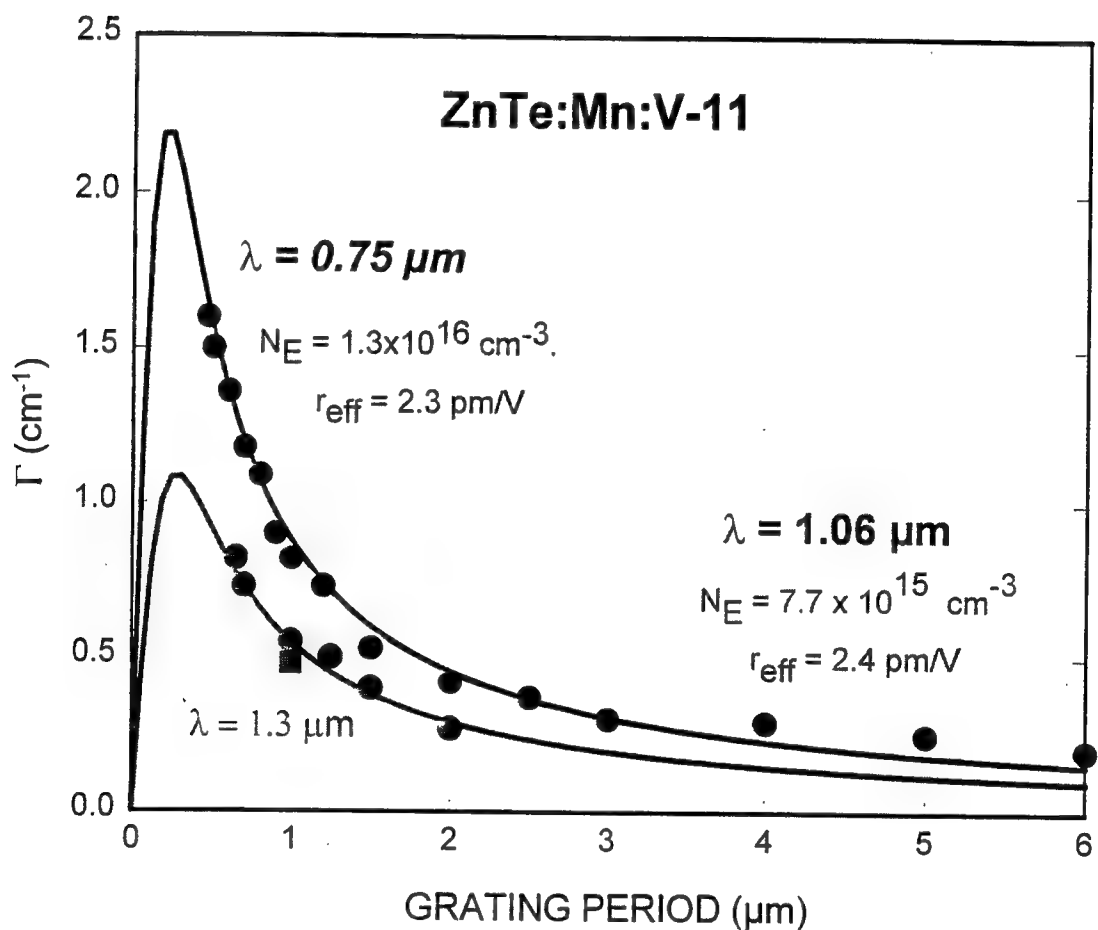


Fig. 5.2. Two-wave mixing gain versus grating period at 750 nm and 1064 nm wavelengths. The solid line is a fit of the single-trap single carrier model.

---

mixing. Experiments were carried out between 633nm and 1523 nm. The samples were photorefractive over this wavelength range. Results of the two-wave mixing experiments at 750 nm are shown in Fig. 5.2. The solid line is a fit of the single carrier, single trap model. these results yield a trap density of  $N_e = 1.3 \times 10^{16} \text{ cm}^{-3}$  and  $r_{\text{eff}} = 2.3 \text{ pm/V}$ . The trap density is over two orders of magnitude larger than previously reported in ZnTe:V. The electro-optic coefficient is about 2/3 of the expected value, possibly due to electron-hole competition. Two-wave mixing measurements carried out at other wavelengths did not indicate any significant decrease or reversal of the gain direction.

## 5.2 CdMnTe:V

$\text{Cd}_{1-x}\text{Mn}_x\text{Te}$  was considered also as a candidate photorefractive material for the near infrared. The band gap of  $\text{Cd}_{1-x}\text{Mn}_x\text{Te}$  varies with mole fraction  $x$  as  $1.53 + 1.26x$  eV[14].  $\text{Cd}_{0.55}\text{Mn}_{0.45}\text{Te}$  crystals doped with vanadium were grown by the vertical Bridgman technique.  $\text{Cd}_{0.55}\text{Mn}_{0.45}\text{Te}$  has a band gap of 2.1eV.

A single crystal sample of  $5 \times 5 \times 5$  mm<sup>3</sup> dimensions with  $<110>x<110>x<100>$  orientation was used for these experiments. Gold electrodes were deposited on each of the (001) faces. The sample had a large dark resistivity of  $> 10^9$  ohm-cm. The absorption spectrum is shown in Fig. 5.3. The absorption tail extended from about 0.6  $\mu\text{m}$  to beyond 1.5 $\mu\text{m}$ .

Photorefractive two-beam coupling was observed from 0.63 $\mu\text{m}$  to 1.5 $\mu\text{m}$ . Measurements of the two-beam coupling gain coefficient versus grating period at 0.75 $\mu\text{m}$  wavelength is shown in Fig. 5.4. The solid line is a fit of the single carrier, single trap model. This fit gives an electro-optic coefficient of 2.5 pm/V, which is close to the measured value of 2.8 pm/V we obtained by measuring the electro-optic retardation of a weak probe beam. The fit also gives a value of  $N_e = 1.3 \times 10^{15}$ .

The dependence of the two-beam coupling gain coefficient on intensity, measured for a 1  $\mu\text{m}$  grating period is shown in Fig. 5.5. The gain was independent of intensity above 0.5 mW/cm<sup>2</sup>. Fig. 5.6 shows the intensity dependence of the response time at 1  $\mu\text{m}$  grating period.

The two-beam coupling gain was also measured for applied square wave ac electric fields. Fig. 5.7 shows the dependence of gain on grating period for a 7 kV/cm applied electric field. Fig. 5.8 shows the dependence on ac field frequency for an input intensity of 6 mW/cm<sup>2</sup> and an applied field of 7 kV/cm and 10  $\mu\text{m}$  grating period. The gain showed the expected frequency dependence, and not the fall off at higher frequencies as was seen in BSO.

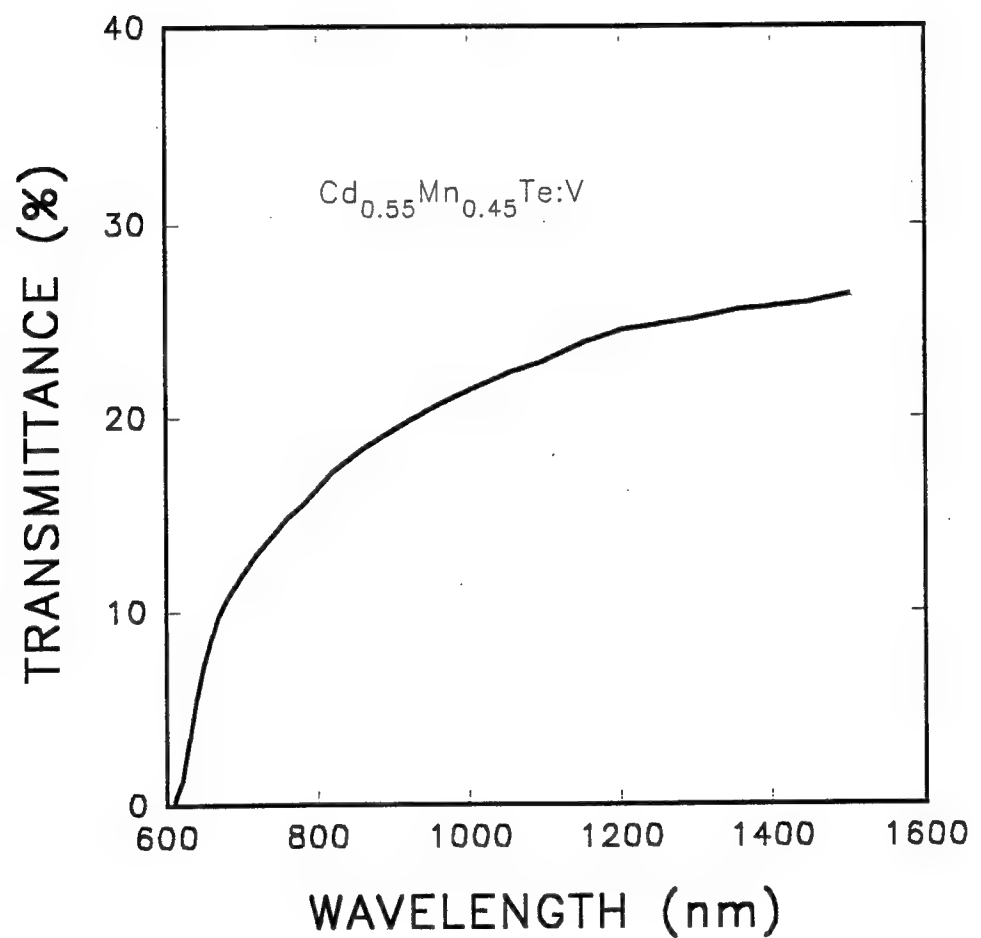


Fig. 5.3. Absorption spectrum of  $\text{Cd}_{0.55}\text{Mn}_{0.45}\text{Te:V}$ .

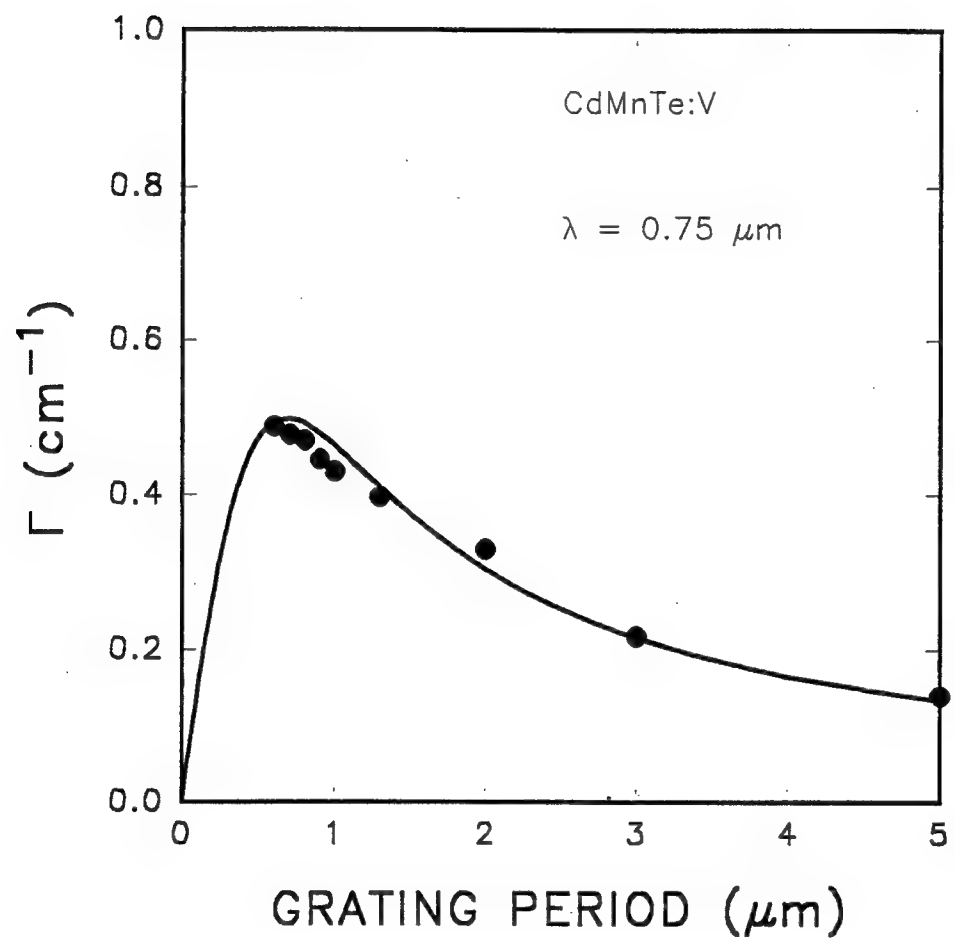


Fig. 5.4. Two-wave mixing gain versus grating period at 750 nm wavelength. The solid line is a fit of the single-trap single-carrier model.

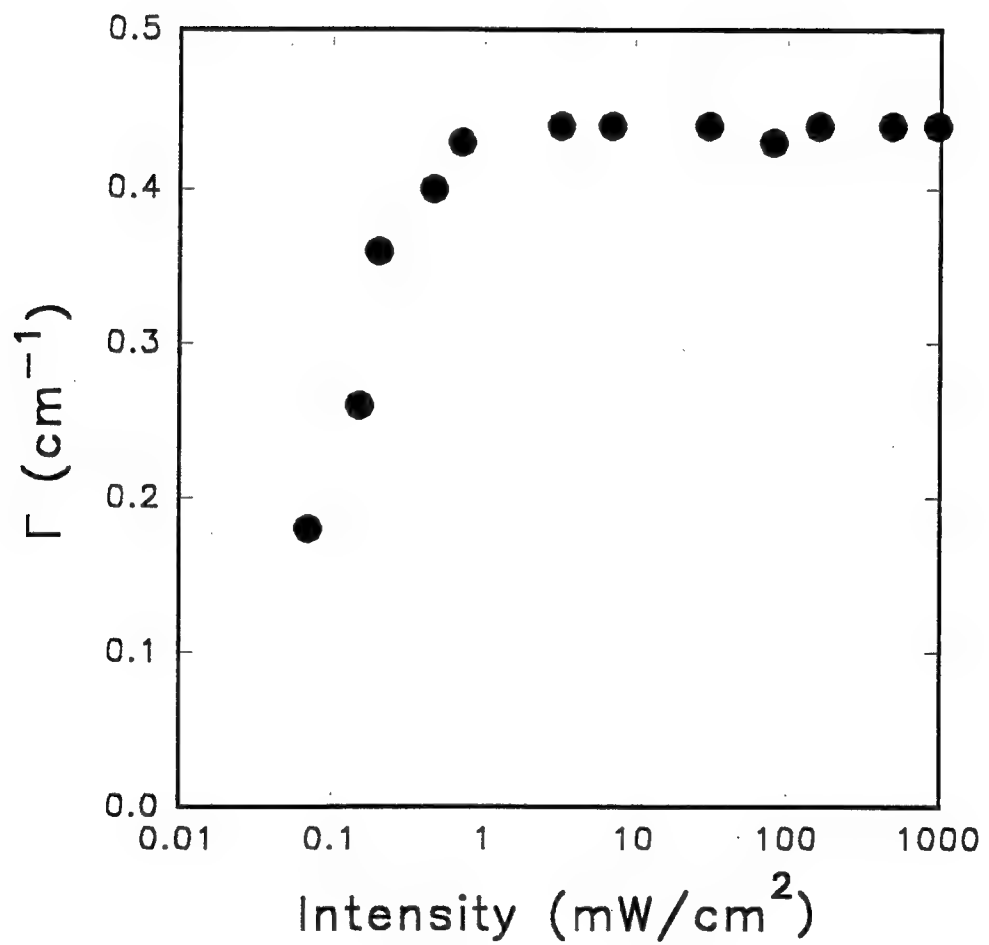


Fig. 5.5. Two-beam coupling gain versus incident intensity for  $\text{Cd}_{0.55}\text{Mn}_{0.45}\text{Te:V}$ .

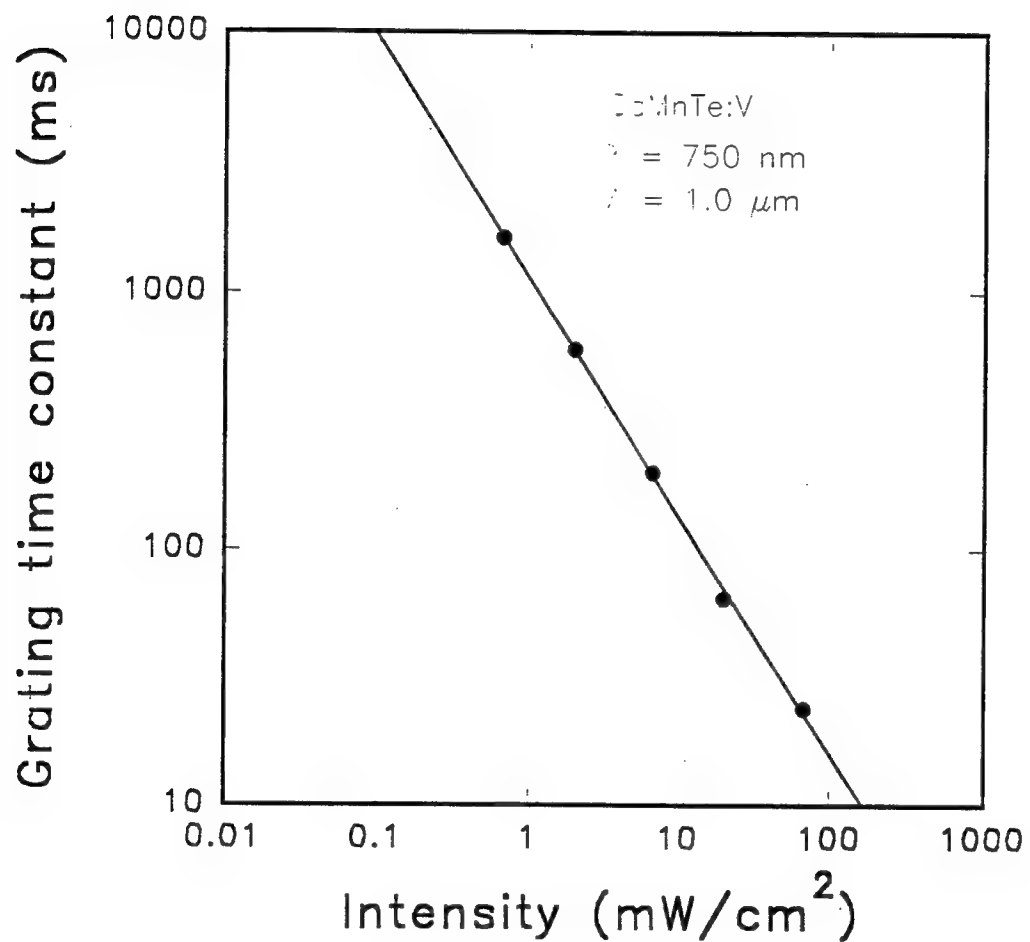


Fig. 5.6. Grating formation response time versus incident intensity for  $\text{Cd}_{0.55}\text{Mn}_{0.45}\text{Te:V}$ .

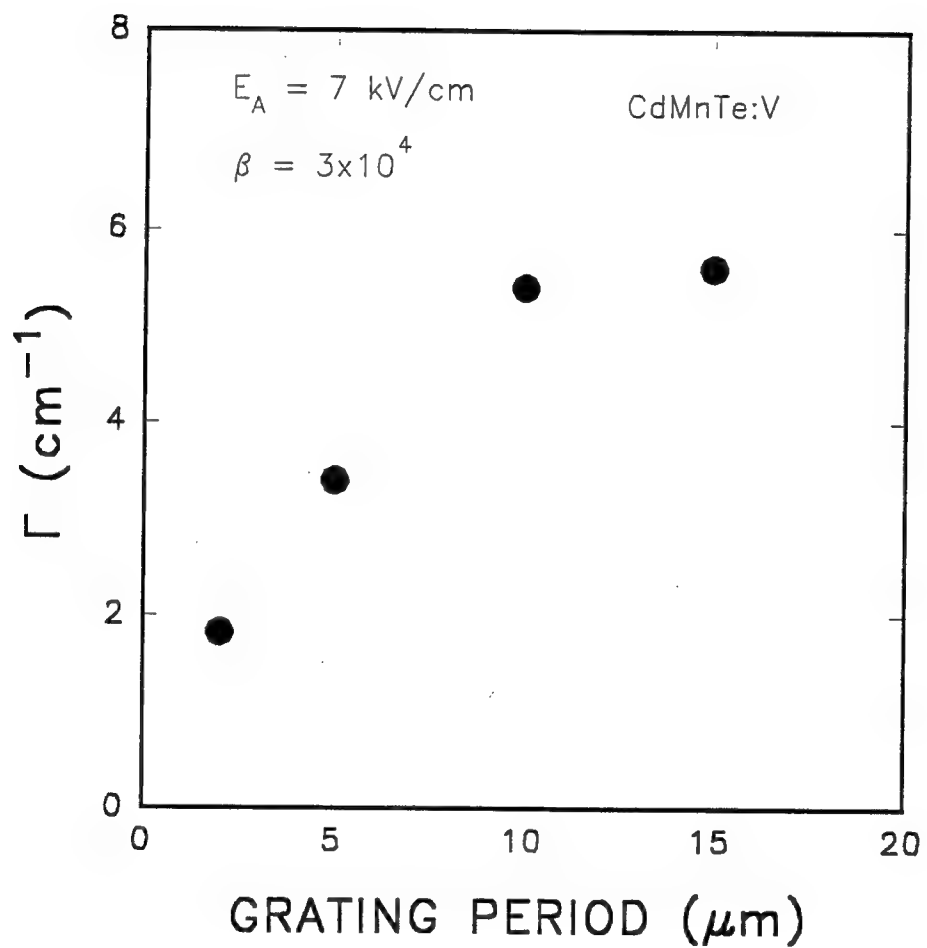


Fig. 5.7. Two-wave mixing gain versus grating period in  $\text{Cd}_{0.55}\text{Mn}_{0.45}\text{Te:V}$  with an applied ac field.

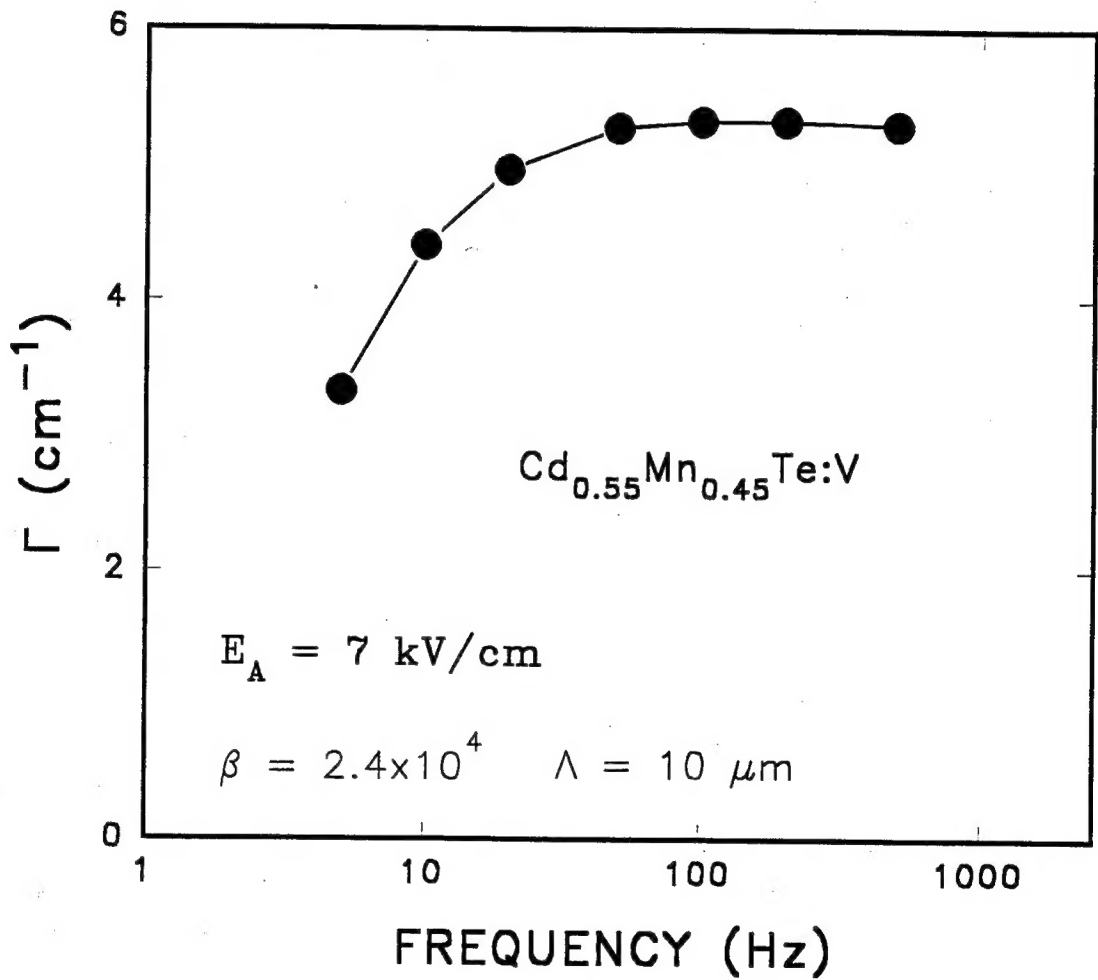


Fig. 5.8. Two-wave mixing gain versus ac field frequency in  $\text{Cd}_{0.55}\text{Mn}_{0.45}\text{Te:V}$ .

## 6. SUMMARY

The photorefractive effect can be utilized in optical signal processing applications, such as an optical integrating element in a radar signal processor. Numerical and experimental studies were conducted to determine performance characteristics of semiconductor photorefractives for such applications. The nonstationary recording techniques of moving gratings and alternating electric fields offer the potential of significant enhancement over that which could be obtained with a dc field under stationary recording conditions. However, there are significant deviations from the linearized theory. The modulation dependencies of the photorefractive response were investigated. For applications for which the modulation depth is less than about 0.1 these techniques can provide useful enhancements. In both the moving grating and the ac field techniques, the large enhancements in diffraction efficiency at large modulation are not fully realized, due to saturation of the space-charge field.

In the case of the moving grating technique, the photorefractive response has a complicated dependence on both modulation and fringe velocity. The optimum fringe velocity for diffraction at large modulation is a value that is much slower than for the small modulation regime. The grating phase also depends upon modulation and fringe velocity. This variation in phase with modulation would not be acceptable for radar signal processing.

The alternating electric field technique looks to be a viable technique. It is possible to approximate the numerical solutions with analytical expressions, and easily predict the performance characteristics. Although the space charge field does saturate at large modulation, at  $m = 1$ , the space charge field is still about 20% larger than could be obtained with a dc field alone. The main difficulty with the ac field technique is the requirement on the frequency of the high voltage signal generator. Our studies indicate that the ac field frequency should satisfy the condition that  $Q > 50$  for phase stability less than 1%. In the case of BSO, a decrease in the photorefractive response was observed for

moderate ac frequencies. This effect is not fully understood, and merits additional attention.

The photorefractive response was also investigated for the stationary conditions of a dc applied field. The numerical and experimental results show that the photorefractive response exhibits a superlinear behavior with modulation. This enhanced steady-state response comes at the expense of an additional time requirement. A significant increase in time is required to reach steady-state at  $m = 1$  than at small modulation. The oscillatory behavior can be damped at large modulation.

II-VI materials exhibit good potential as photorefractories for operation in the near infrared. The photorefractive response in ZnTe was improved by co-doping with Mn and V. By co-doping, the effective trap concentration was increased by about two orders of magnitude over that with vanadium doping alone. This is significant, since the value of  $N_E \approx 10^{14} \text{ cm}^{-3}$  ZnTe:V was considered to be insufficient for photorefractive applications. The absorption coefficient in this material is large. Additional studies are needed to determine the optimum doping levels. CdMnTe was examined as an alternative to ZnTe. CdMnTe:V exhibited good photorefractive response and good optical quality. An effective trap concentration of  $N_E \approx 10^{15} \text{ cm}^{-3}$  was measured.

## REFERENCES

1. P.K. Das and C. DeCusatis, *Acousto-Optic Signal Processing*, Artech House, Boston, 1991.
2. A. Vanderlugt, *Optical Signal Processing*, Marcel Dekker, New York, 1992.
3. D. Psaltis, J. Yu, J. Hong, *Appl. Opt.* **24**, 3860 (1985).
4. W. Penn, RADC-TR-86-188, (1986).
5. P. Refregier, L. Solymar, H. Rajbenbach, and J.P. Huignard, *J. Appl. Phys.* **58**, 45 (1985).
6. S.I. Stepanov and M.P. Petrov, in *Photorefractive Materials and Their Applications I*, P. Gunter and J.P. Huignard, eds. (Springer Verlag, New York, 1988).
7. K. Walsh, A.K. Powell, C. Stace, and T.J. Hall, *J. Opt. Soc. Am B* **7**, 288 (1990).
8. B. Imbert, H. Ragbenbach, S. Mallic, J.P. Herriau, and J. P. Huignard, *Opt. Lett.* **13**, 327 (1988).
9. G.A. Swinburne, T.J. Hall, and A.K. Powell, *IEEE Proceedings of the International Conference on Holographic Systems, Components, and Applications*, (Institution of Electrical Engineers, London, 1989).
10. L.B. Au and L. Solymar, *J. Opt. Soc. Am. A* **7**, 1154 (1990).
11. L.B. Au and L. Solymar, *Opt. Lett.* **13**, 660 (1988).
12. N.V. Kukhtarev, V.B. Markov, S.G. Odoulov, and V.L. Vinetskii, *Ferroelectrics*, **22**, 949 (1979).
13. M. Ziari, W.H. Steier, P.M. Ranon, S. Trivedi, and M.B. Klein, *Appl. Phys. Lett.*, **60**, 1052 (1992).
14. P. Lautenshlager, S. Logothetidis, L. Vina, and M. Carona, *Phys. Rev. B* **32**, 3811 (1985).